RESEARCH ARTICLE

Open Access

Geochemical characteristics of back-arc basin lower crust and upper mantle at final spreading stage of Shikoku Basin: an example of Mado Megamullion

Norikatsu Akizawa[1*] , Yasuhiko Ohara[2,3,4], Kyoko Okino[1], Osamu Ishizuka[5], Hiroyuki Yamashita[6], Shiki Machida[7], Alessio Sanfilippo[8], Valentin Basch[8], Jonathan E. Snow[9], Atlanta Sen[9,10], Ken-ichi Hirauchi[11], Katsuyoshi Michibayashi[4], Yumiko Harigane[5], Masakazu Fujii[12], Hisashi Asanuma[1] and Takafumi Hirata[13]

Abstract

This paper explores the evolutional process of back-arc basin (BAB) magma system at final spreading stage of extinct BAB, Shikoku Basin (Philippine Sea) and assesses its tectonic evolution using a newly discovered oceanic core complex, the Mado Megamullion. Bulk and in-situ chemical compositions together with in-situ Pb isotope composition of dolerite, oxide gabbro, gabbro, olivine gabbro, dunite, and peridotite are presented. Compositional ranges and trends of the igneous and peridotitic rocks from the Mado Megamullion are similar to those from the slow- to ultraslow-spreading mid-ocean ridges (MOR). Since the timing of the Mado Megamullion exhumation corresponds to the very end of the Shikoku Basin opening, the magma supply was subdued and highly episodic, leading to extreme magma differentiation to form ferrobasaltic, hydrous magmas. In-situ Pb isotope composition of magmatic brown amphibole in the oxide gabbro is identical to that of depleted source mantle for mid-ocean ridge basalt (MORB). In the context of hydrous BAB magma genesis, the magmatic water was derived solely from the MORB source mantle. The distance from the back-arc spreading center to the arc front increased away through maturing of the Shikoku Basin to cause MORB-like magmatism. After the exhumation of Mado Megamullion along detachment faults, dolerite dikes intruded as a post-spreading magmatism. The final magmatism along with post-spreading Kinan Seamount Chain volcanism were introduced around the extinct back-arc spreading center after the opening of Shikoku Basin by residual mantle upwelling.

Keywords: Gabbro, Peridotite, Oceanic core complex, Magmatic water, In-situ Pb isotope, And Slab rollback

1 Introduction

Back-arc basins (BAB) are extensional basins formed behind subduction zones by rifting and in some cases, seafloor spreading developing on the overriding plate. Arc magmatism has been investigated intensively because it is a general feature of every subduction zone setting and significantly hazardous with explosive volcanoes due to the high volatile contents in the arc magmas (e.g., Tatsumi and Suzuki-Kamata 2014), while the BAB are not always present in the subduction zones and make up far less of Earth's surface compared to open ocean basins. Considering that the BAB belong to the same regional setting as the arcs and contributes significantly to the dynamics of subduction zones [cf. review by Pearce and Stern (2006)], it is significant to examine magma genesis in BAB as a step toward the understanding of the magmatic system in convergent margins.

*Correspondence: akizawa@aori.u-tokyo.ac.jp
[1] Atmosphere and Ocean Research Institute, The University of Tokyo, 5-1-5 Kashiwanoha, Kashiwa, Chiba 277-8564, Japan
Full list of author information is available at the end of the article

BAB basalts (BABB) show a wide variety of chemical composition, which is generally intermediate between mid-ocean ridge basalts (MORB) and island-arc basalts (IAB) (e.g., Gill 1976; Hawkins and Melchior 1985). The IAB-type BABB are characterized by increased concentrations of large ion lithophile elements (LILE) and reduced concentrations of high field strength elements (HFSE): the former is linked to elemental transport by the hydrous fluid, and the latter is linked to increased mantle melting as the result of the hydrous fluid influx (e.g., Stolper and Newman 1994; Pearce and Stern 2006). The introduction of water in the mantle wedge lowers its solidus, allowing mantle melting to greater extents at a given temperature (e.g., Hirschmann et al. 1999; Parman and Grove 2004), which in turn leading to the formation of highly refractory residual peridotites. Accordingly, modern-day peridotites from forearcs are significantly more chemically depleted than most mid-ocean ridge peridotites (Parkinson and Pearce 1998; Pearce et al. 2000; Birner et al. 2017). The subduction-related elemental input and mantle depletion associated with BABB genesis have also been documented by perspectives from isotopes, halogens, and noble gasses (e.g., Hickey-Vargas 1991; Ikeda et al. 1998; Pearce et al. 1999; Kendrick et al. 2020). These data are also in good agreement with geophysical investigations that depicted a thicker and more differentiated BAB crust located close to the arc, as a consequence of enhanced mantle melting caused by hydrous fluid supply from the down-going slab (Arai and Dunn 2014; Eason and Dunn 2015). The gradual decrease in IAB signature with increasing distance from the arc reflects the maturing of the BAB (Taylor and Martinez 2003; Langmuir et al. 2006).

Previous studies on BAB focused mainly on basaltic samples from the shallow crust as they are more accessible than to the lower crust and underlying mantle samples. Hence, plutonic rocks and peridotites from these settings are poorly studied although they can be of critical importance to investigate nascent magmatic system at the BAB. Oceanic core complexes (OCC), dome-like features representing footwalls of detachment faults (i.e., large-offset extensional fault with low-angle surface expressions), are important tectonic windows into the lower crust and uppermost mantle beneath oceanic spreading systems (e.g., Cann et al. 1997). These features can locally occur in BAB, where they allow for a direct investigation of deep-seated materials. For instance, recent studies on the Godzilla Megamullion, the world's largest OCC ($\sim 125 \times 55$ km^2) located in an extinct BAB, the Parece Vela Basin (Philippine Sea) (Ohara et al. 2001, 2002, 2003; Harigane et al. 2011, 2019; Loocke et al. 2013; Sanfilippo et al. 2013). As a whole, the gabbro, troctolite and peridotite

from the Godzilla Megamullion are similar to those from the mid-ocean ridges (MOR) in terms of petrography and chemistry. More recently, Harigane et al. (2019) evidenced a functional necessity of magma-derived water to parental magmas of gabbros from the Godzilla Megamullion. Similar conclusions were reached by Basch et al. (2020) for the lower crustal rocks of a newly discovered OCC, named Mado Megamullion in the Shikoku Basin (Philippine Sea). Based on textural and chemical characteristics of a subset of gabbros and troctolites, Basch et al, (2020) suggested that the involvement of primary magmas enriched in water in the Shikoku Basin–Parece Vela Basin magma system as a functional necessity to generate abundant amphibole in the lower crust in the BAB. In detail, Basch et al. (2020) argued that the abundant water in the primary magmas contributed to the precipitation of clinopyroxenes at a very early stage of the BAB magma evolution, followed by Fe-Ti oxides and pargasitic amphiboles in the evolved gabbros. Although the efforts toward unraveling early evolutionary process of "wet" BAB magma system, the mechanism driving water enrichment is still equivocal due to later multiple metamorphic overprints under the presence of seawater (e.g., Harigane et al. 2019). To tackle this issue, in-situ analysis of isotope sensitive to seawater introduction into the magmatic body must be coupled to careful petrographic observation. In addition, since the BAB magma changes in composition during the maturing of BAB as mentioned above, we need to reassess the water involvement during the course of BAB evolution, considering that both the Mado Megamullion and Godzilla Megamullion formed at the final spreading stage of Shikoku Basin and Parece Vela Basin, respectively.
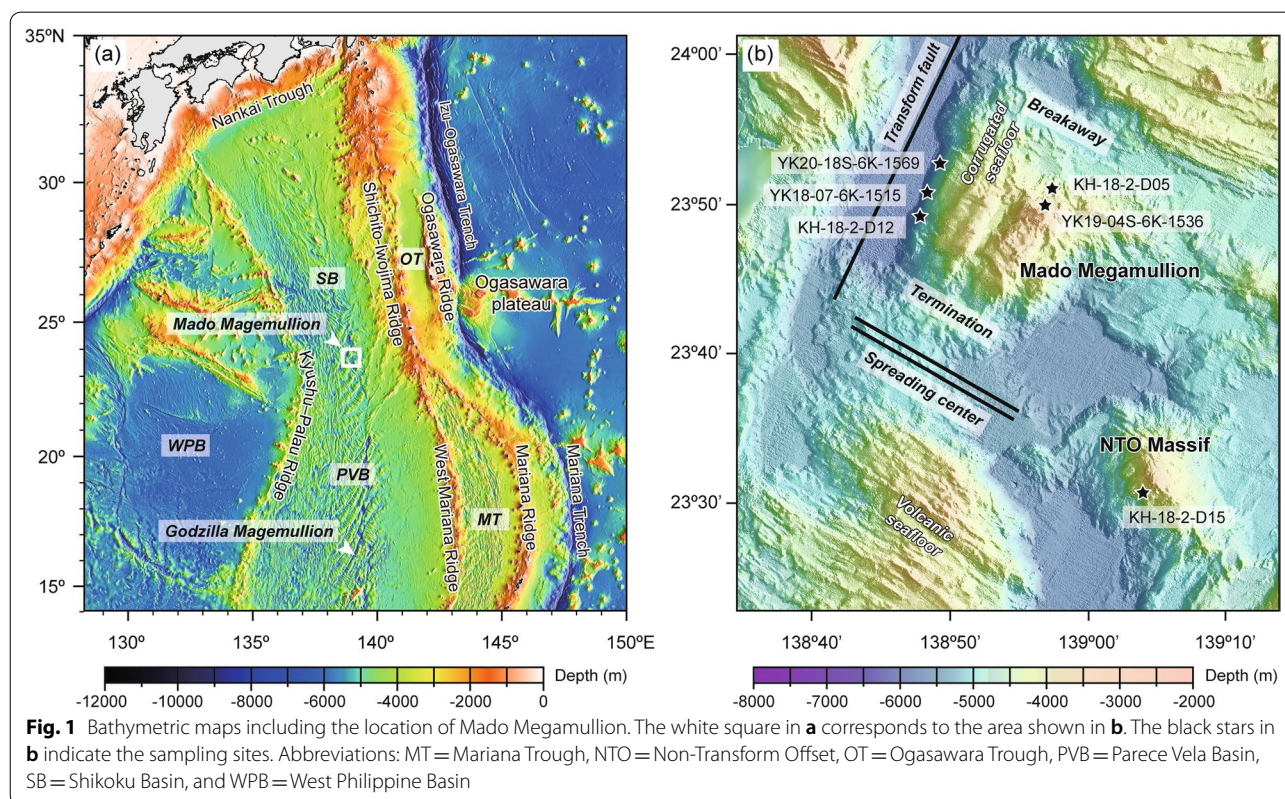
Here, we present bulk and in-situ chemical compositions, combined with in-situ Pb isotope composition of crustal and mantle rocks collected at the Mado Megamullion. Recently, Basch et al. (2020), Hirauchi et al. (2021), and Sen et al. (under review) have been reporting in-situ mineral compositions of the rock samples collected at the Mado Megamullion, but their bulk chemical composition and isotope composition have not yet been analyzed to date. The main aims of this study are to investigate mantle melting, magma transport, and wet BAB magma evolution, and to perceive the tectonic evolution of the Shikoku Basin, with analyzing bulk and in-situ chemical compositions together with in-situ Pb isotope composition of the rock samples from the Mado Megamullion. In principle, we consider that the timing of the exhumation of Mado Megamullion corresponds to the very end of the spreading of Shikoku Basin, where subdued, episodic magmatism is supposed beneath the back-arc spreading center.

2 Geological background

The Shikoku Basin is a broad fan-shaped BAB at the northern end of the Philippine Sea bounded by the Kyushu–Palau Ridge to the west, the Izu–Ogasawara island arc–trench system to the east, and the Nankai Trough to the north (Fig. 1a). The Shikoku Basin merges to the north of the Parece Vela Basin at ca. 24°S (Fig. 1a). A geodynamic evolution of the Shikoku Basin was reconstructed using magnetic anomalies and topography by Okino et al. (1994) and later revised based on newly collected geophysical data by Okino (2015). Four stages can be recognized and synthetized as follows. (1) The formation of the Shikoku Basin initiated with the rifting in the Early Oligocene followed by the opening from ca. 24 Ma. This initial stage corresponds to the final volcanic stage of Kyushu–Palau Ridge (Ishizuka et al., 2011). (2) A mature ocean floor opened in NNW-SSE direction from ca. 24 to 22 Ma with southward propagation of the Shikoku Basin spreading center at a speed of ca. 10 cm/year. The spreading rate was estimated at ca. 2.3 cm/year in the beginning, then increased to ca. 4.6 cm/year. (3) The spreading axis gradually rotated clockwise to N-S from ca. 22 to 19 Ma. The spreading rate was estimated at ca. 4.5 cm/year, then decreased down to 2.3 cm/year. (4) The spreading axis was gradually rotated anticlockwise to NW–SE from ca. 19 to 15 Ma. The spreading rate was estimated at ca. 2–3 cm/year before the cessation of the spreading. During the final spreading, the spreading axis was frequently segmented at the scale of few tens of kilometers, and spreading direction was oblique (i.e., sigmoidal or curved).

The extinct spreading center of the Shikoku Basin is overlapped by a volcanic seamounts chain, called Kinan Seamount Chain (Okino et al., 1998, 1999). The Kinan Seamount Chain yields an age range of ca. 15 to 7 Ma (Ishizuka et al., 2009), thus erupted well after the cessation of Shikoku Basin spreading. The estimated tectonic arrangement and the age data indicate that the magmas remained beneath the axial zone caused post-spreading Kinan Seamount Chain volcanism (Okino et al., 1999; Ishizuka et al., 2009). Using multiple isotopic analyses (Pb, Nd and Sr), Sato et al. (2002) and Ishizuka et al. (2009) revealed that the Kinan Seamount Chain basalts show compositional similarity to the MORB with various degree of contribution from enriched mantle component (EM-1). Of note, the Kinan Seamount Chain basalts show limited chemical signatures of subduction-related elemental input (Ishizuka et al., 2009). Toward the southern Shikoku Basin, the size of the seamounts decreases, and the rift structure remains in the remnant spreading axis. The Mado Megamullion is located

Fig. 1 Bathymetric maps including the location of Mado Megamullion. The white square in **a** corresponds to the area shown in **b**. The black stars in **b** indicate the sampling sites. Abbreviations: MT = Mariana Trough, NTO = Non-Transform Offset, OT = Ogasawara Trough, PVB = Parece Vela Basin, SB = Shikoku Basin, and WPB = West Philippine Basin

at an inside corner of ridge axis–transform intersection in the southernmost Shikoku Basin (Fig. 1b).

The multibeam bathymetry of Mado Megamullion shows spreading-parallel surface corrugations on the domed surface, having a typical characteristic of OCC exposed at MOR (Ohara et al. 2018; Okino et al. 2019). The corrugated detachment surface expands over ~ 500 km² until the termination region (Fig. 1b). The Mado Megamullion, along with the other topographic highs in the same region such as Non-Transform Offset (NTO) Massif (Fig. 1b), are found in correspondence with the mantle bouguer anomaly fields ca. 20 mGal higher than the surroundings (Okino et al. 2019; Akizawa et al. 2020a). This is attributed to the presence of high-density materials in the shallow region, consistent with the presence of gabbros or variously serpentinized peridotites (Ohara et al. 2018; Basch et al. 2020; Hirauchi et al. 2021; Sen et al. under review). The gabbros from the Mado Megamullion record crystal-plastic deformation events at granulite-facies (ca. 930–870 °C) to amphibolite-facies (850–810 °C) conditions, which likely commenced in presence of small melt fractions (Basch et al. 2020). The deep-rooted gabbroic and peridotitic rocks from the Mado Megamullion were exhumed to the seafloor via detachment faulting initiated at breakaway region (Fig. 1b).

3 Sampling sites and submersible seafloor observation

In this study, we used rock samples collected at the Mado Megamullion by seafloor dredging during R/V Hakuho-maru KH-18-2 cruise, and by submersible diving using deep-submergence vehicle (DSV) Shinkai 6500 during R/V Yokosuka YK18-07, YK19-04S, and YK20-18S cruises. The samples were collected along the transform fault (KH-18-2-D12, YK18-07-6K-1515, and YK20-18S-6K-1569), and on the top of the dome-like structure of the Mado Megamullion (KH-18-2-D05, YK19-04S-6K-1536) (Fig. 1b). We observed exclusively angular gabbroic outcrops in the domed top (Fig. 2a), whereas smooth peridotitic outcrops with platy dike intrusions and angular gabbroic rocks were observed along the wall of the transform fault (Fig. 2b) during submersible observation by DSV Shinkai 6500. In addition to the Mado Megamullion, we dredged rock samples from the NTO Massif (KH-18-2-D15, Fig. 1b), which also has the dome-like structure.

4 Sample description

A total of 19 igneous rocks and 15 peridotitic rocks were selected for our study. They are classified as dolerite, oxide gabbro, gabbro, olivine gabbro, dunite, and peridotite (Table 1). Modal proportions of the rocks were determined by point counting method with covering the area of entire thin section (about 4.7×2.8 cm²). Modal amounts of primary orthopyroxene and clinopyroxene were not estimated for the peridotites as most of them are completely altered to bastite pseudomorphs (Hirauchi et al. 2021) and indistinguishable from each other. For this reason, we use the general rock name peridotite, instead of harzburgite or lherzolite.

The dolerites are mainly composed of lath-shaped plagioclase and granular clinopyroxene with trace amounts of euhedral to subhedral Fe-Ti oxide and granular brown amphibole (Fig. 3a). The minerals are fine-grained (~ 1 mm in diameter) and show ophitic texture. The dolerites are particularly devoid of deformation.

The oxide gabbros are coarse-grained (~ 1 cm in diameter) and show hypidiomorphic texture (Figs. 2c, 3b). Clinopyroxene and plagioclase are often rimmed by pale brown to green amphibole and chlorite, respectively (Figs. 3b, 4). Brown amphibole is present as granular or interstitial to clinopyroxene and plagioclase (Fig. 3b). Rare fine-grained (~ 0.1 mm in diameter) subhedral titanite is in close association with the amphibole. In place, a mylonitic YK20-18S-6K-1569-R4-2 oxide gabbro is directly in contact with a porphyroclastic YK20-18S-6K-1569-R4-1 olivine gabbro (Fig. 2d).

Main constituent mineral of the olivine gabbros and gabbros are plagioclase and clinopyroxene with minor olivine, Fe-Ti oxide, amphibole, and orthopyroxene (Table 1). The olivine gabbros and gabbros show a deformation intensity grading from undeformed to mylonitic through porphyroclastic, and constituent mineral grain size comes to 1 cm in diameter (Table 1). Orthopyroxene is intimately associated with olivine (Fig. 3c). Interstitial to granular brown amphibole is frequently replaced by green amphibole (Fig. 3d). In the less deformed samples, micrometer-sized brown amphibole veinlets crosscut magmatic minerals such as plagioclase and clinopyroxene, and a part of brown amphibole is in general replaced by the green amphibole (Fig. 3d). Mylonitic YK19-04S-6K-1536-R14B-2 olivine gabbro shows a sharp contact with porphyroclastic YK19-04S-6K-1536-R14B-1 gabbro (Fig. 3e). Textural variability is recognized in KH-18-2-D05-R101A-a olivine gabbro: fine-grained (~ 1 mm in diameter) domains are enclosed within a granular coarse-grained (~ 5 mm in diameter) domain (Fig. 3f). Such gabbroic rocks are called varitextured gabbro and interpreted as a mixture of gabbro with frozen melts crystallized in-situ in the periphery of axial melt lens (e.g., Koepke et al., 2011; Basch et al. 2020). Some gabbros are crosscut by centimeter to millimeter-sized felsic veins, which are locally organized in a framework disrupting a former gabbro and thereby called hybridized gabbro (Basch et al. 2020). Their parental melts are preferentially
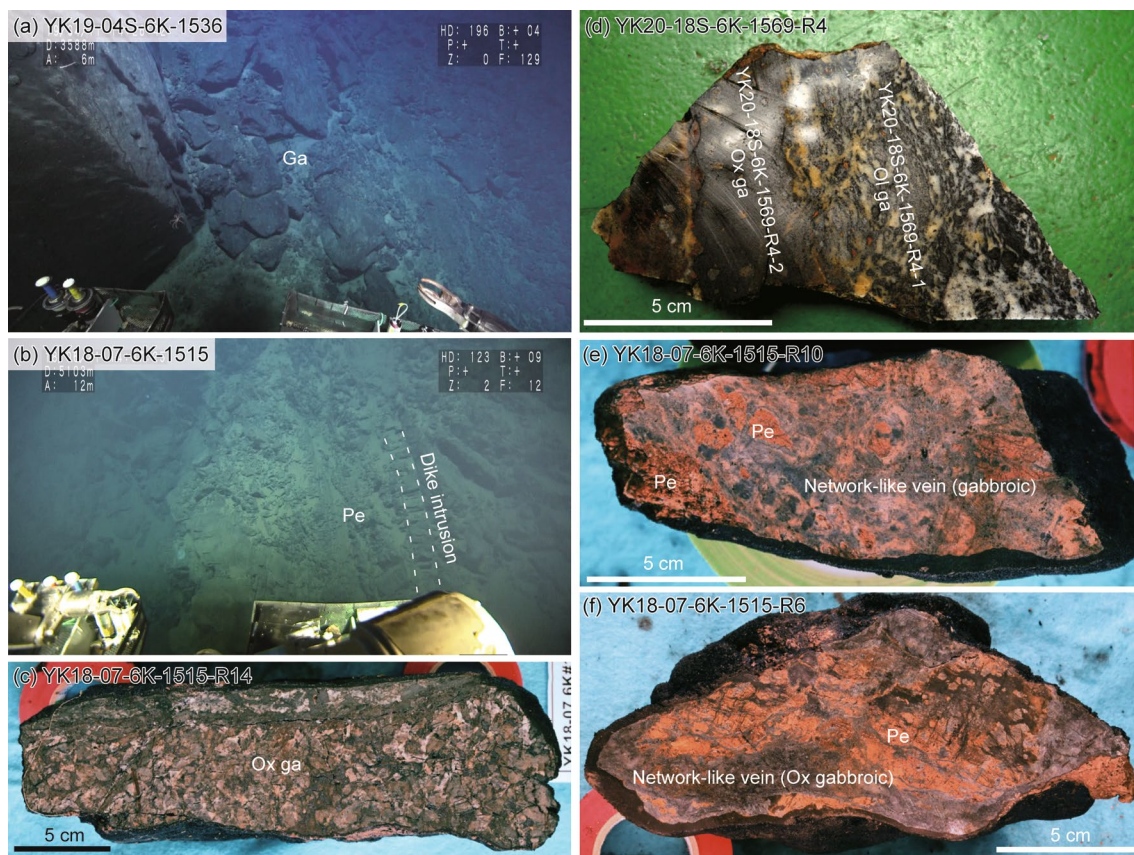
Fig. 2 Seafloor observation and rock samples from Mado Megamullion. **a** Representative occurrence of gabbroic rocks on the seafloor. **b** Representative occurrence of peridotitic rocks with platy dike intrusion on the seafloor. **a**, **b** were taken during submersible diving of 6K-1536 and 6K-1515, respectively. **c** YK18-07-6K-1515-R14 oxide gabbro. **d** A contact between YK20-18S-6K-1569-R4-1 gabbro and YK20-18S-6K-1569-R4-2 oxide gabbro. **e** YK18-07-6K-1515-R10 peridotite with gabbroic vein network. **f** YK18-07-6K-1515-R6 peridotite with oxide gabbroic vein network. Abbreviations: Ga = gabbro, Ol ga = olivine gabbro, Ox ga = oxide gabbro, and Pe = peridotite

interpreted to have been generated by extreme differentiation of magma, although an origin by hydrous partial melting of gabbros under amphibolite facies cannot be excluded (Basch et al. 2020).

The dunites and peridotites are severely serpentinized (Table 1). In the dunites, chromian spinel is subhedral in shape (Fig. 3g) and more abundant (2.6–6.4 vol%) than in the peridotites (~1.9 vol%) (Table 1). Orthopyroxene and bastite pseudomorphs after pyroxenes are often associated with the chromian spinel in the dunites (Fig. 3g). Some peridotites include vermicular-shaped chromian spinel within the orthopyroxene or bastite pseudomorphs after pyroxenes (Fig. 3h, Table 1). Of note, some peridotites are crosscut by centimeter to millimeter-sized network-like veins (Figs. 2e, 2f, 3i). The network-like veins are mainly composed of clinopyroxene, plagioclase, and brown amphibole with trace Fe-Ti oxide. The plagioclase and clinopyroxene-rich veins are referred to as "gabbroic veins," whereas the brown amphibole and plagioclase-rich veins are referred to as "oxide gabbroic veins," hereafter (Table 1). In the hand specimens, these veins can be distinguished by color contrast: dark greenish for the gabbroic vein (Fig. 2e) and blackish for the oxide gabbroic vein (Fig. 2f). The oxide gabbroic veins are particularly abundant in the brown amphibole, which is in part replaced or overgrown by green amphibole with close association of chlorite (Fig. 3k). The orthopyroxene and clinopyroxene are, respectively, replaced by pale brown to green amphibole and talc (Fig. 3j), and pale brown to green amphibole around the veins. Kinked orthopyroxene porphyroclasts exhibit undulose extinction with neoblasts in YK18-07-6K-1515-R3 peridotite (Fig. 3l).

5 Analytical methods
5.1 Bulk major-element analysis
Sample powders were prepared by a procedure described in our previous report by Akizawa et al. (2020b). For bulk

Table 1 Summary of sample information

Sample name	Lithology	Depth (m)	Latitude	Longitude	Maximum grain size (mm)	Mode (vol%)							Comment
						Ol	Pl	Cpx	Ox	Amp	Opx	Total	
YK18-07-6K-1515-R8	Dolerite	5490	23°50.5850′ N	138°48.0841′ E	1	–	57.4	36.8	2.6	3.2	–	100	
YK18-07-6K-1515-R11	Dolerite	5162	23°50.4648′ N	138°48.3606′ E		Not measured							
YK18-07-6K-1515-R12	Dolerite	5162	23°50.4648′ N	138°48.3606′ E	0.5	–	66.2	29.7	2.7	1.4	–	100	
YK18-07-6K-1515-R13	Dolerite	5162	23°50.4648′ N	138°48.3606′ E	0.5	–	66.6	29.1	3.4	1.0	–	100	
YK20-18S-6K-1569-R7a	Dolerite	5713	23°53.3793′ N	138°49.0433′ E		Not measured							
YK20-18S-6K-1569-R10	Dolerite	5713	23°53.3793′ N	138°49.0433′ E		Not measured							
YK18-07-6K-1515-R4	Oxide gabbro	5599	23°50.6100′ N	138°47.9940′ E	10	–	51.0 [a]	27.0 [a]	15.0 [a]	7.0 [a]	–	100	Coarse-grained
YK18-07-6K-1515-R14	Oxide gabbro	5073	23°50.4372′ N	138°48.3942′ E	10	–	46.2	29.6	14.1	10.1	–	100	Coarse-grained
YK20-18S-6K-1569-R4-2	Oxide gabbro	5713	23°53.3793′ N	138°49.0433′ E		Not measured							Mylonitic. Contact with YK20-18S-6K-1569-R4-1
YK20-18S-6K-1569-R6	Oxide gabbro	5713	23°53.3793′ N	138°49.0433′ E		Not measured							Mylonitic
YK20-18S-6K-1569-R8a	Oxide gabbro	5713	23°53.3793′ N	138°49.0433′ E		Not measured							Mylonitic
YK19-04S-6K-1536-R18	Olivine gabbro	3540	23°49.6782′ N	138°56.6738′ E	3	9.8	54.9	25.2	0.5	7.6	2.0	100	Interstitial brown amphibole and opx
KH-18-2-D05-R101A-a	Olivine gabbro	4522	23°51.7310′ N	138°57.8930′ E	5	1.0 [a]	58.0 [a]	36.0 [a]	–	5.0 [a]	–	100	Varitextured
YK20-18S-6K-1569-R4-1	Olivine gabbro	5713	23°53.3793′ N	138°49.0433′ E		Not measured							Mylonitic. Contact with YK20-18S-6K-1569-R4-2
YK19-04S-6K-1536-R14B-2	Olivine gabbro	3608	23°49.7226′ N	138°56.6931′ E	3	2.8	55.4	26.3	3.2	12.3	–	100	Mylonitic. Contact with YK19-04S-6K-1536-R14B-1
KH-18-2-D05-R101B-1	Gabbro	4522	23°51.7310′ N	138°57.8930′ E	2	–	49.5	43.0	1.1	6.5	–	100	
YK19-04S-6K-1536-R14B-1	Gabbro	3608	23°49.7226′ N	138°56.6931′ E	10	–	63.7	24.4	–	11.9	–	100	Porphyroclastic. Contact with YK19-04S-6k-1536-R14B-2
YK19-04S-6K-1536-R16	Gabbro	3608	23°49.7226′ N	138°56.6931′ E	5	–	36.9	49.2	–	13.9	–	100	Porphyroclastic
KH-18-2-D05-R101B-2	Hybridized gabbro	4522	23°51.7310′ N	138°57.8930′ E	10	–	71.9	18.0	2.9	7.2	–	100	See Basch et al. (2020) for sample photo

Sample name	Lithology	Depth (m)	Latitude	Longitude	Mode (vol%)							Comment
					Ol	Ser	Opx	Cpx	Bas	Spl	Total	
KH-18-2-D12-R7-2	Dunite	5403	23°49.3060′ N	138°47.6350′ E	–	96.9	0.3	–	0.3	2.6	100	Massive spl. Opx presents in association with spl
KH-18-2-D12-R12	Dunite	5403	23°49.3060′ N	138°47.6350′ E	–	93.5	–	–	0.1	6.4	100	Massive spl. Spherical ser inclusion in spl after olivine
KH-18-2-D12-R32B	Dunite	5403	23°49.3060′ N	138°47.6350′ E	–	89.7	–	–	6.6	3.8	100	Massive spl. Bas presents in association with spl
KH-18-2-D12-R2	Peridotite	5403	23°49.3060′ N	138°47.6350′ E	–	71.8	–	–	27.5	0.7	100	Vermicular spl in association with bastite
KH-18-2-D12-R6	Peridotite	5403	23°49.3060′ N	138°47.6350′ E	–	72.3	11.7	–	15.3	0.7	100	Vermicular spl in association with bastite
KH-18-2-D15-R1	Peridotite	5271	23°28.5670′ N	139°02.6920′ E	–	76.1	–	–	23.0	0.9	100	Deformed opx
YK18-07-6K-1515-R3	Peridotite	5680	23°50.6599′ N	138°47.9216′ E	0.3	76.4	14.0	0.1	7.2	1.9	100	Vermicular spl. Deformed opx

Table 1 (continued)

Sample name	Lithology	Depth (m)	Latitude	Longitude	Mode (vol%)							Comment
					Ol	Ser	Opx	Cpx	Bas	Spl	Total	
KH-18-02-D12-R4	Peridotite	5403	23°49.3060′ N	138°47.6350′ E	–	83.3	7.8	–	7.9	1.0	100	Network-like vein (oxide gabbroic)
KH-18-02-D12-R15	Peridotite	5403	23°49.3060′ N	138°47.6350′ E	–	82.4	4.0	–	13.1	0.4	100	Deformed opx. Network-like vein (oxide gabbroic)
YK18-07-6K-1515-R2	Peridotite	5680	23°50.6599′ N	138°47.9216′ E	–	87.8	0.5	–	11.5	0.2	100	Network-like vein (oxide gabbroic)
YK18-07-6K-1515-R6	Peridotite	5490	23°50.5850′ N	138°48.0841′ E	Not measured							Network-like vein (oxide gabbroic)
YK18-07-6K-1515-R9	Peridotite	5295	23°50.5202′ N	138°48.2549′ E	–	83.4	0.6	–	15.6	0.4	100	Vermicular spl. Network-like vein (oxide gabbroic)
YK18-07-6K-1515-R10	Peridotite	5295	23°50.5202′ N	138°48.2549′ E	Not measured							Network-like vein (gabbroic)
YK18-07-6K-1515-R15	Peridotite	5032	23°50.4233′ N	138°48.4398′ E	Not measured							Network-like vein (gabbroic)
YK19-04S-6K-1536-R12A	Peridotite	3748	23°49.8227′ N	138°56.7323′ E	Not measured							Network-like vein (oxide gabbroic)

Ol, olivine; Pl, plagioclase; Cpx, clinopyroxene; Ox, Fe–Ti oxide; Amp, amphibole; Opx, orthopyroxene; Bas, bastite; spl, chromian spinel

[a] Refered to Basch et al. (2020)

major-element analysis, the sample powders were dried for 12 h at 110 °C in an oven. Then, the resulting sample powders were weighed with accuracy of 0.0001 g (W_1 g) and heated for 7 h at 950 °C in a maffle furnace. After the heating procedure, samples were weighed again with accuracy of 0.0001 g (W_2 g) to calculate an ignition loss (loss on ignition: LOI) using the following equation.

$$LOI = (W_1 - W_2)/W_1 \times 100 \, (wt\%) \tag{1}$$

Fused-glass beads were prepared from the sample powders used for the LOI measurements. After the mixing of sample powder (0.4000 ± 0.0004 g) with a 4.0000 ± 0.0004 g flux ($Li_2B_4O_7$, MERCK), the resulting sample mixture was fused for 600 s at 1180 °C within a Pt-Au crucible with 3.5 cm in diameter (95% Pt and 5% Au) using a RIGAKU automated high frequency bead sampler at Atmosphere and Ocean Research Institute (AORI), the University of Tokyo (Kashiwa, Japan) (Akizawa et al., 2020b). After the cooling, the resulting fused-glass beads were analyzed for bulk major elements.

Bulk major-element composition (SiO_2, TiO_2, Al_2O_3, Cr_2O_3, total $Fe_2O_3 = TFe_2O_3$, MnO, MgO, CaO, Na_2O, K_2O, NiO, and P_2O_5) of the fused-glass bead was determined using a RIGAKU ZSX Primus II X-ray fluorescence (XRF) spectrometer at AORI. An accelerating voltage of 50 kV and a probe current of 50 mA were employed for the XRF measurements. Calibration curves were determined with geological reference materials of JA-1 (andesite), JA-2 (andesite), JA-3 (andesite), JB-1b (basalt), JB-2 (basalt), JB-3 (basalt), JCh-1 (chert), JF-1 (feldspar), JF-2 (feldspar), JG-1a (granodiorite), JG-2 (granite), JG-3 (granodiorite), JGb-1 (gabbro), JGb-2 (gabbro), JH-1 (hornblendite), JLk-1 (lake sediment), JSd-1 (stream sediment), JSd-2 (stream sediment), JSd-3 (stream sediment), JSl-1 (slate), JSl-2 (slate), JSy-1 (syenite), JP-1 (dunite), JR-1 (rhyolite), JR-2 (rhyolite), JR-3 (rhyolite), and JP-1+JB-2 (a mixture with the ratio of 1:1) distributed from Geological Survey of Japan (GSJ). The abundance values for the analytes were referred from compiled reference reported by Imai et al. (1995, 1996,

1999). Reference materials of AGV-1 (andesite), BIR-1 (basalt), DNC-1 (diabase), STM-1 (syenite), and W-2 (diabase) obtained from United States Geological Survey (USGS) were also analyzed to evaluate the accuracy of the resulting data. The results of the reference materials are consistent with the reference values given by Gladney and Roelandts (1988a, b), and Jochum et al. (2016) (see Additional file 1: Table S1).

5.2 Mineral major-element analysis

Major-element compositions of minerals were determined with an electron probe micro-analysis (EPMA) using a JEOL JXA-8900R microprobe installed at AORI. An accelerating voltage of 15 kV, a probe current of 12 nA, and a beam diameter of 3 μm were adopted. A peak counting time of 20 s and a background counting time of 10 s were used, except for Na and Ni, for which a peak counting time of 10 s and a background counting time of 5 s, and a peak counting time of 30 s and a background counting time of 15 s were used, respectively. Natural or synthetic minerals of quartz (SiO_2), potassium titanium phosphate ($KTiPO_4$), corundum (Al_2O_3), eskolaite (Cr_2O_3), manganosite (MnO), periclase (MgO), wollastonite ($CaSiO_3$), manganese ferrite ($MnO¬Fe_2O_3$), jadeite ($NaAlSi_2O_6$), and nickel oxide (NiO) were used as standards. Raw data were corrected using a ZAF online correction program. Mg# was calculated as $Mg/(Mg + Fe^{2+})$ atomic ratio, and An content as $Ca/(Ca + Al + K)$ atomic ratio for plagioclase.

5.3 Bulk trace-element analysis

Concentrations of trace elements Li, V, Rb, Sr, Y, Zr, Nb, Cs, Ba, La, Ce, Pr, Nd, Sm, Eu, Gd, Tb, Dy, Ho, Er, Tm, Yb, Lu, Hf, Ta, Pb, Th and U were determined by inductively coupled plasma-mass spectrometry (ICP-MS) utilizing an Agilent 7900 ICP-MS installed at the Geological Survey of Japan (GSJ/AIST, Japan). About 100 mg of sample powder was decomposed by a mixture of HF and HNO_3 (3:1) in a Teflon beaker using a microwave dissolution system (Anton Paar Mutiwave 3000). The dissolved

(See figure on next page.)

Fig. 3 Petrography of rock samples from Mado Megamullion. **a** Granular brown amphibole in YK18-07-6K-1515-R8 dolerite. **b** Coarse-grained YK18-07-6K-1515-R14 oxide gabbro. The white squares show analytical area by EPMA in Fig. 4. **c** Interstitial brown amphibole and orthopyroxene in YK19-04S-6K-1536-R18 olivine gabbro. **d** Interstitial brown amphibole overprinted by green amphibole in YK19-04S-6K-1536-R18 olivine gabbro. **e** A contact between porphyroclastic YK19-04S-6K-1536-R14B-1 olivine gabbro and mylonitic YK19-04S-6K-1536-R14B-2 olivine gabbro. **f** Varitextured YK18-2-D05-R101-a olivine gabbro. **g** Anhedral massive chromian spinel in KH-18-02-D12-R32b dunite. **h** Vermicular chromian spinel in bastite pseudomorph after orthopyroxene in KH-18-02-D12-R2 peridotite. **i** Network-like vein in YK19-04S-6K-1536-R12A peridotite. The white square represents the area of **k**. **j** Partial replacement of orthopyroxene by pale brown amphibole and talc close to network-like vein in YK18-07-6K-1515-R6 peridotite. **k** Overgrowth of green amphibole on brown amphibole in network-like vein in YK19-04S-6K-1536-R12A peridotite. **l** Kinked orthopyroxene porphyroclast exhibiting undulose extinction with neoblasts in YK18-07-6K-1515-R3 peridotite. **a**, **f**, **h**, **i** and **l** were taken under crossed-polarized light. **b**, **c**, **d**, **e**, **g** and **k** were taken under plane-polarized light. **j** is COMP image taken by EPMA. Abbreviations: Amp = amphibole, Ba = bastite, Chl = chlorite, Cpx = clinopyroxene, Dol = dolerite, Du = dunite, Ga = gabbro, Ol = olivine, Ol ga = olivine gabbro, Opx = orthopyroxene, Ox ga = oxide gabbro, Pe = peridotite, Pl = plagioclase, Pm = pseudomorph, Ser = serpentine, Spl = chromian spinel, and Tlc = talc
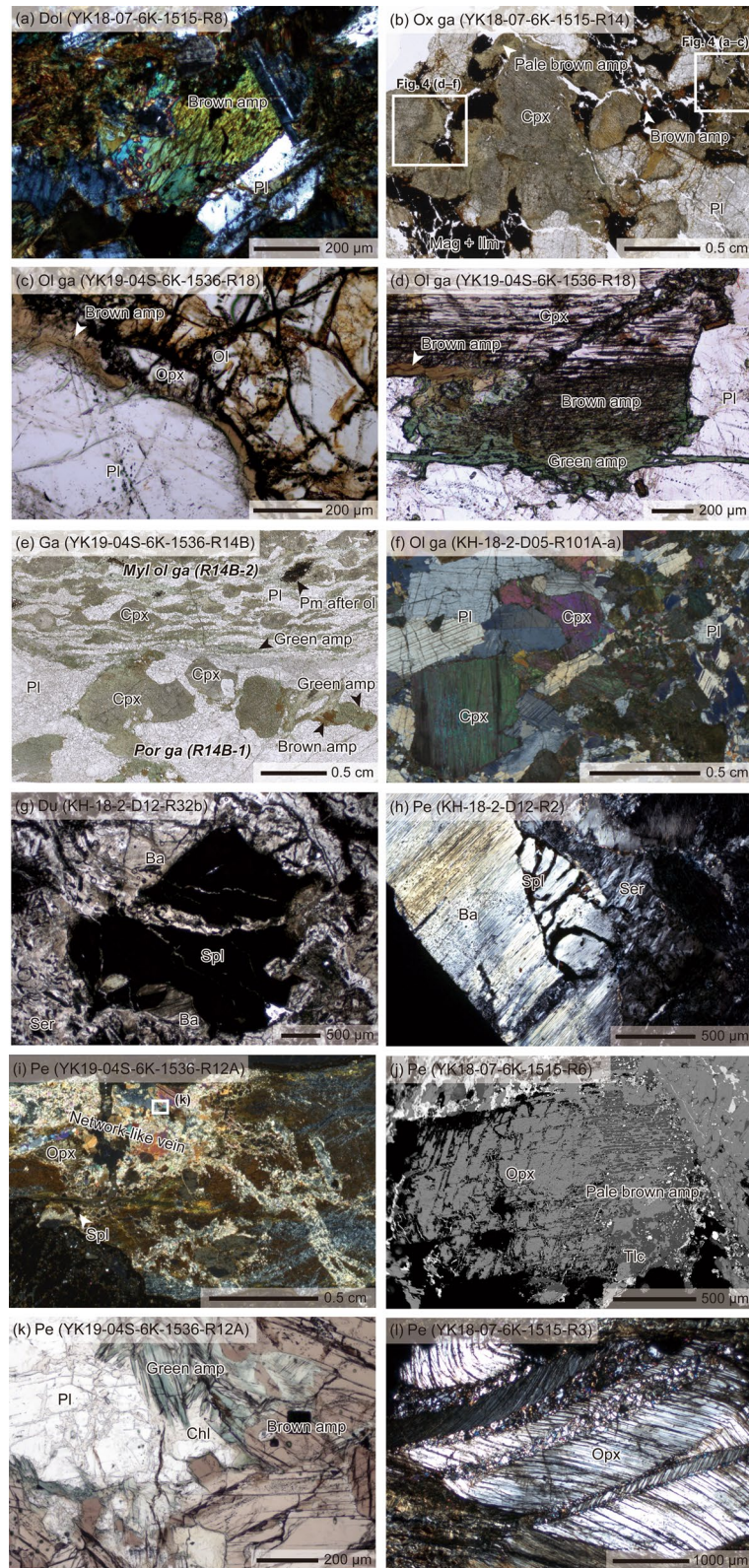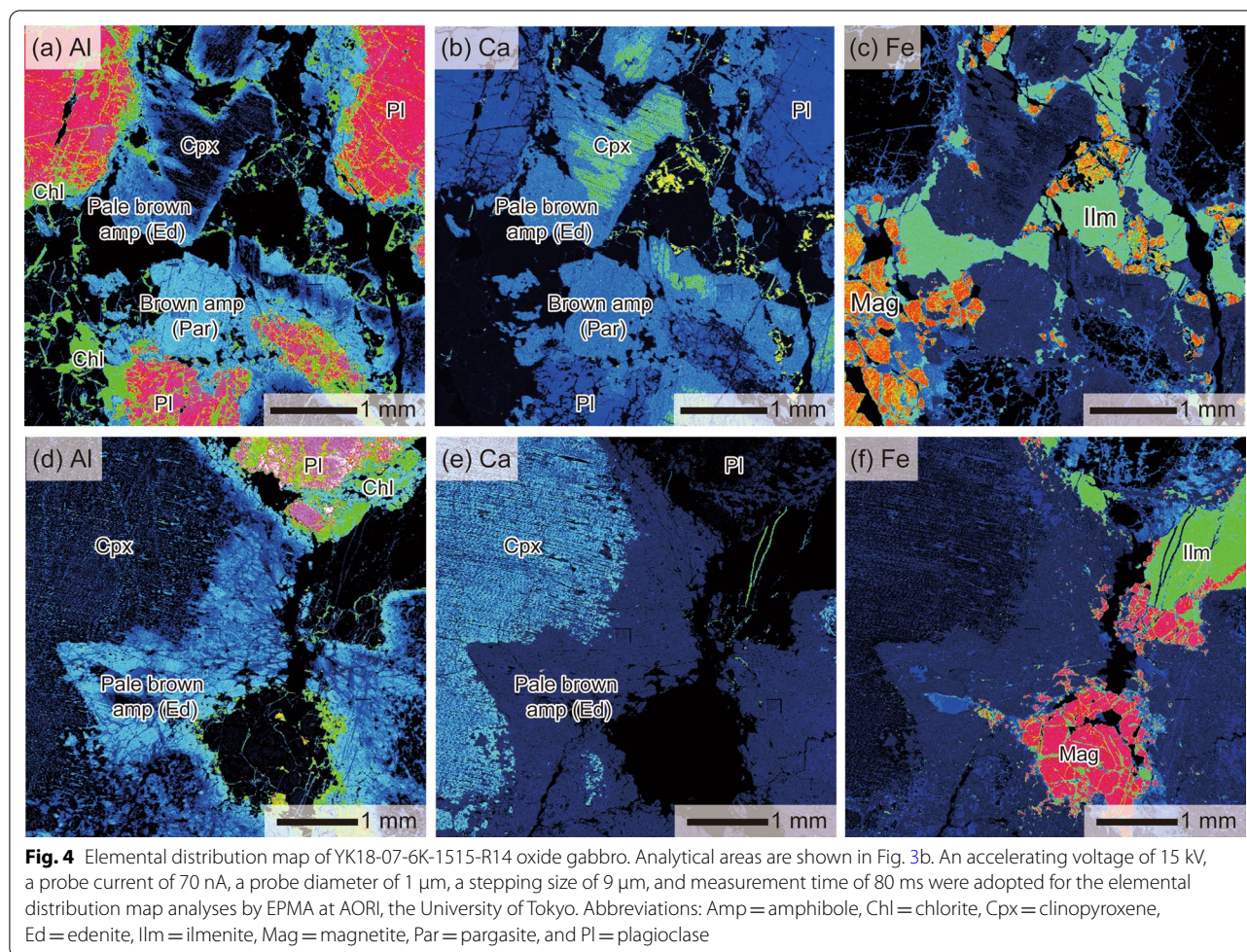
Akizawa *et al. Progress in Earth and Planetary Science*   (2021) 8:65

Page 9 of 24

Fig. 3 (See legend on previous page.)

Fig. 4 Elemental distribution map of YK18-07-6K-1515-R14 oxide gabbro. Analytical areas are shown in Fig. 3b. An accelerating voltage of 15 kV, a probe current of 70 nA, a probe diameter of 1 μm, a stepping size of 9 μm, and measurement time of 80 ms were adopted for the elemental distribution map analyses by EPMA at AORI, the University of Tokyo. Abbreviations: Amp = amphibole, Chl = chlorite, Cpx = clinopyroxene, Ed = edenite, Ilm = ilmenite, Mag = magnetite, Par = pargasite, and Pl = plagioclase

sample solutions were then heated to dryness, and the sample cakes were re-dissolved in 2% HNO_3 prior to the ICP-MS analysis. Indium and Re were used for internal standardization, while JB-2 basalt solution with similar dilution to the sample was used as external standard during ICP-MS measurements. Instrumental calibration was carried out using five to six solutions made from international rock standard materials of BIR-1, BCR-1, AGV-1, JB-1a, JA-1, and JGb-1. Reproducibilities of the measurements were generally better than ± 4% (2 SD) for the rare-earth elements (REE), and better than ± 6% (2 SD) for other elements except for trace elements with very low concentrations (Ishizuka et al. 2020; see BHVO-2 analyses in Additional file 1: Table S2). Detection limits vary from element to element, but for elements with low concentrations such as REE and Ta typically were 0.2 to 2 pg g^{-1}.

5.4 In-situ Pb isotope analysis

In-situ Pb isotope analysis was conducted by a double-focusing   multiple-collector-ICP-MS   (MC-ICP-MS)

(Neptune XT, Thermo Fisher Scientific) combined with a laser ablation system utilizing 260 nm femtosecond laser (Jupiter solid nebulizer, ST Japan INC.) installed at the University of Tokyo (Hongo, Japan). The laser ablation system enables us laser sampling with ultrafast laser scanning achieved by combination of a Galvanometric optics and high-repetition rate (> 1 kHz) (Yokoyama et al. 2011; Makino et al. 2019). In-situ Pb isotope analysis was carried out by laser ablation of 200×200 μm^2 area with a repetition rate of 4000 Hz and with an energy density (fluence) of 4.4 kJ/cm^2 at the target area. We used a He gas with flow rate of 0.6 l/min as a carrier gas to enhance both the production of small sample aerosols and minimizing re-deposition of the sample aerosol around the ablation pit (Eggins et al. 1998; Günther and Heinrich 1999), resulting in better transport efficiency from the sample cell to the ICP and better ionization efficiency. An Ar makeup gas was added at the exit of the sample cell at a flow rate of 1.0 l/min. A signal-smoothing device was set between the sample cell and the torch to improve signal stability (Tunheng and Hirata 2004). Optimum

instrumental parameters were established to show a maximum Pb intensity using a standard of NIST SRM 610. In the MC-ICP-MS analysis, amplifiers utilizing 10^{13} Ω resistor were applied to two Faraday detectors for ^{202}Hg (L3) and ^{204}Pb (L1) isotopes. For Faraday detectors for other three isotopes ^{206}Pb (H1), ^{207}Pb (H2), and ^{208}Pb (H3), conventional amplifiers utilizing 10^{11} Ω resistor were applied. Detailed analytical conditions are summarized in Additional file 1: Table S3.

Signal intensities for Pb isotopes were monitored with time-resolved analysis (TRA) mode. Integration times of 5 s and 10 s were employed for background and analyte signals, respectively. A sample-standard-sample bracketing technique was employed for mass bias calibration. A single analytical session is composed of 3 spot analyses of the NIST SRM610 glass, and about 12 spot analyses of unknown samples or the basaltic reference BIR-1G glass. The mass bias was calibrated with normalizing ^{208}Pb/^{206}Pb and ^{207}Pb/^{206}Pb ratios of the NIST SRM610 glass based on the literature values reported by Woodhead and Hergt (2001). For data reduction, a conventional tau correction method was utilized to compensate decay in signal response (Kimura et al. 2016). We calculated a mean of individual ratio along with a standard deviation of the mean. A total uncertainty of ^{208}Pb/^{206}Pb and ^{207}Pb/^{206}Pb ratios sum statistical errors from the standard deviation of the mean and the repeatability of primary standard analyses. The resultant ^{208}Pb/^{206}Pb and ^{207}Pb/^{206}Pb ratios for the BIR-1G glass were agreed well with the reference values reported by Elburg et al. (2005) (Additional file 1: Table S4).

6 Results

6.1 Bulk major-element analysis

Bulk major-element compositions are given in Additional file 1: Table S5 with total amounts of sample powder prepared in this study. The igneous rocks show chemical correlations as in Fig. 5a–c, which include chemical compositions of igneous and peirdotitic rocks from the global MOR system. The peridotites with the gabbroic and oxide gabbroic veins are deviated from normal depleted peridotites (Fig. 5). The deviations are shown with the pale blue and black arrows in Fig. 5a, b.

6.2 Mineral major-element analysis

Mineral major-element compositions were analyzed for selected samples and are shown in Additional file 1: Tables S6–11. The clinopyroxenes in the peridotite show higher Mg# value (∼0.9) and Cr_2O_3 content (∼1.0 wt%) than those in the igneous rocks (Fig. 6a). The plagioclases in the peridotite overlap in chemical composition to those in the oxide gabbro (Fig. 6b), being consistent with the fact that the plagioclases in the peridotite are a

constituent mineral of the oxide gabbroic vein. In the plagioclase An content–clinopyroxene Mg# space, the Mado Megamullion igneous rocks follow a compositional trend close to that of Southwest Indian Ridge (SWIR) (Fig. 6c). The trend is distinct from that of East Pacific Rise (EPR) or Mid-Atlantic Ridge (MAR) (Fig. 6c). The amphiboles show a wide compositional range from tremolite to pargasite, through hornblende and edenite in the peridotite, olivine gabbro and oxide gabbro (Fig. 6d).
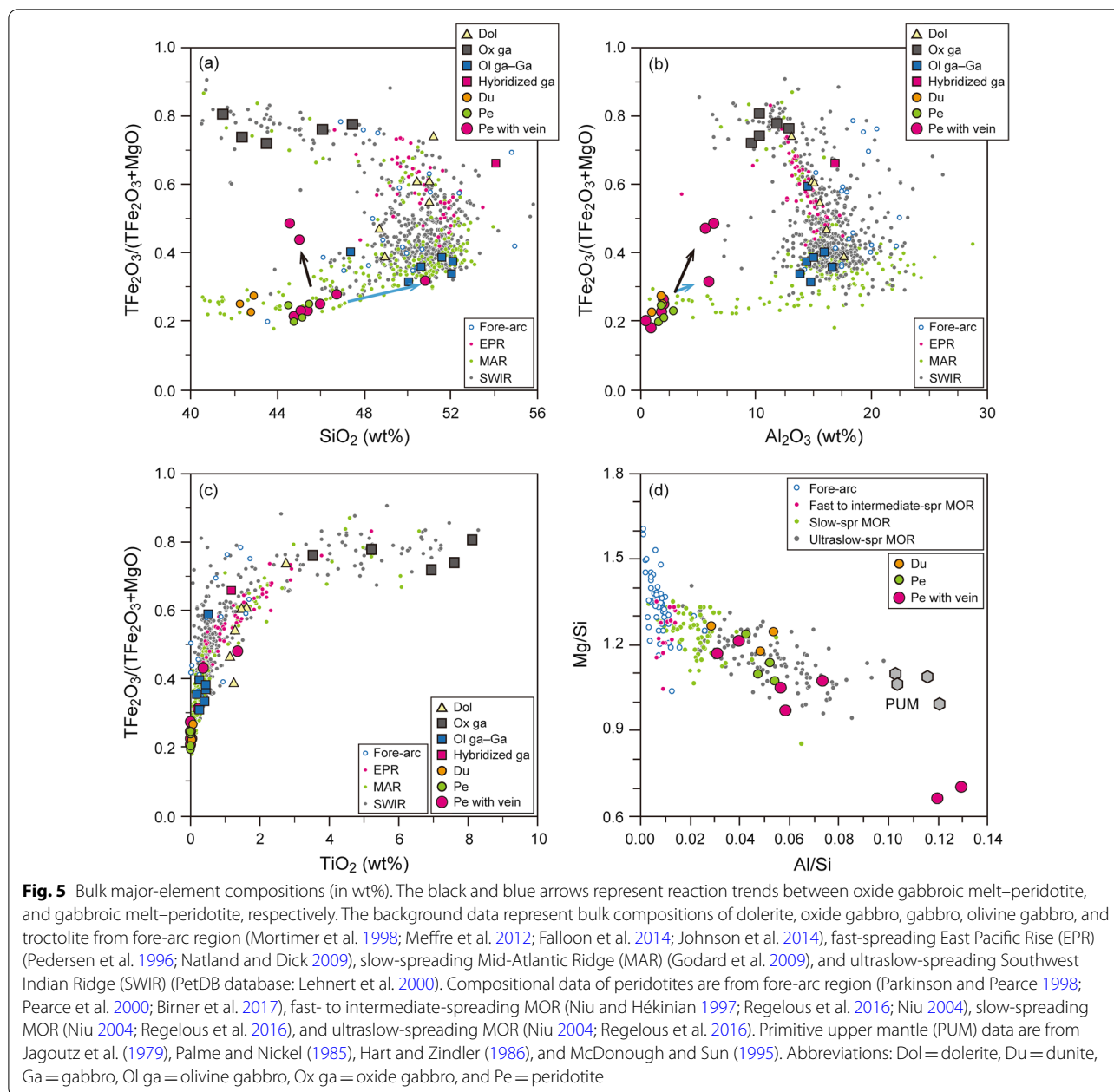
6.3 Bulk trace-element analysis

Bulk trace-element concentrations are given in Additional file 1: Table S5. CI chondrite-normalized trace-element and REE patterns are shown in Fig. 7. The abundances of trace elements are poorer in the gabbro and olivine gabbro than the other igneous rocks (Fig. 7a, b). The ratio of light REE (LREE) and heavy REE (HREE) are higher in the dolerite and hybridized gabbro than the other igneous rocks (La/Yb vs Dy/Yb ratios are shown in Fig. 8). The olivine gabbro and gabbro show positive Eu and Sr anomalies (Fig. 7a). The REE patterns of dolerite are characterized by a steady decrease from middle REE (MREE) to LREE with flatness between MREE and HREE (Fig. 7c). The LREE-rich dolerite shows negative Eu and Sr anomalies (Figs. 7a, 9a). The incompatible trace elements are more abundant in the peridotite associated with the gabbroic and oxide gabbroic veins than in those without these magmatic veins (Fig. 7c, d). The dunite is higher in LREE/HREE ratio and lower in MREE/HREE ratios than the peridotite (La/Yb vs Dy/Yb ratios are shown in Fig. 8). The samples showing compositional anomaly of Ce in the MORB-normalized REE patterns are significantly high in LOI (Fig. 9b).

6.4 In-situ Pb isotope analysis

We analyzed clear crystalline grains of magmatic brown amphibole in YK18-07-6K-1515-R14 oxide gabbro (Additional file 1: Table S12). The results show tight ranges of ^{207}Pb/^{206}Pb (0.866–0.879) and ^{208}Pb/^{206}Pb (2.114–2.123) (Fig. 10). The data field partly overlaps with that of Kinan Seamount Chain basalts, but it is clearly distinct from those of seawaters and marine sediments (Fig. 10). The data range of ^{207}Pb/^{206}Pb overlaps with a value of depleted MORB source mantle (DMM, a hypothetical source reservoir to depleted MORB) (Fig. 10).

7 Discussion

We discuss the magmatic and tectonic evolution of the Shikoku Basin based on the analytical results of the rock samples recovered from the Mado Megamullion hereafter. We start with the magmatic evolution (Sects. 7.1 to 7.3) and mantle melting (Sect. 7.4), followed by post-spreading magmatism (Sect. 7.5) in the Shikoku Basin
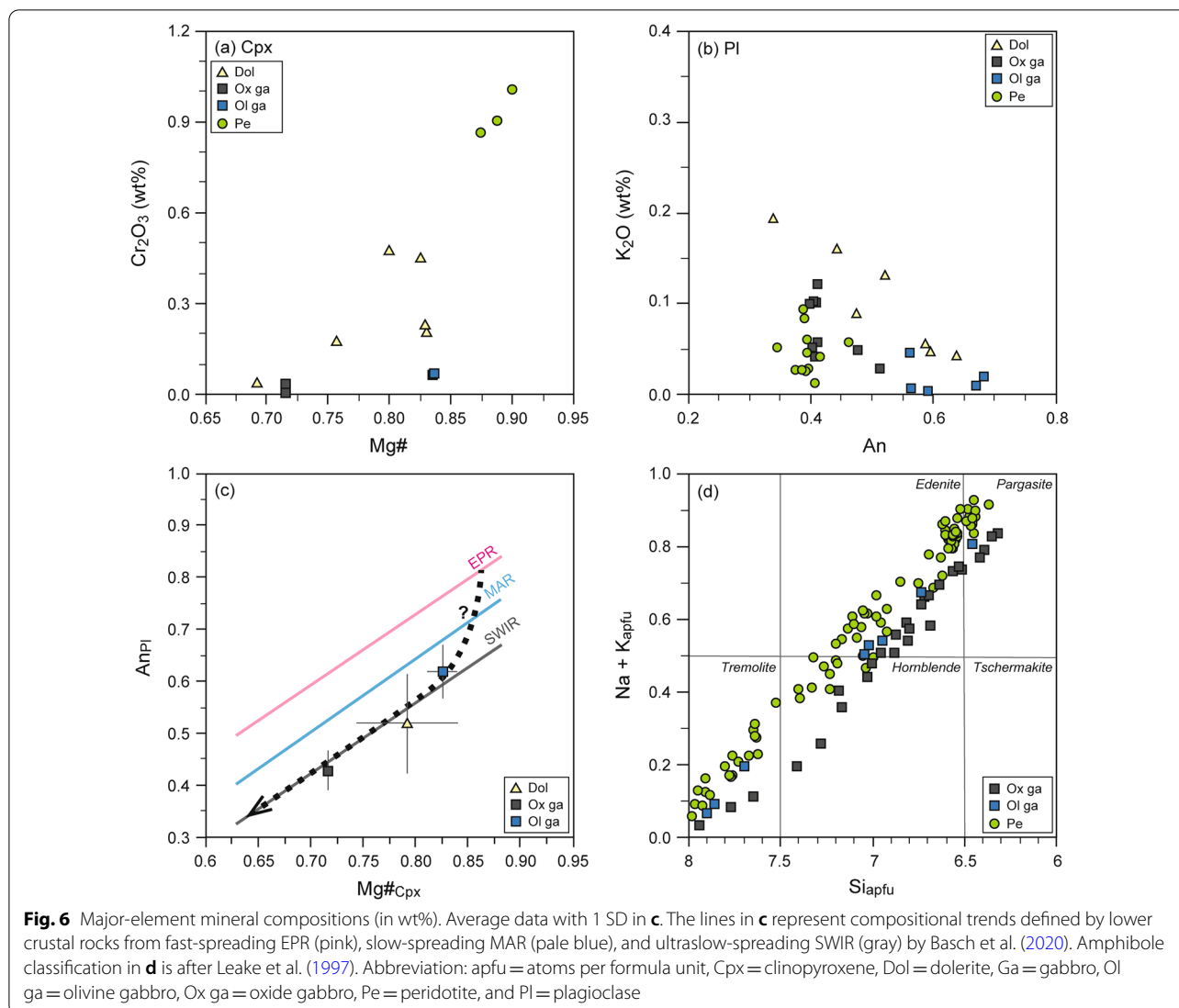
Fig. 5 Bulk major-element compositions (in wt%). The black and blue arrows represent reaction trends between oxide gabbroic melt–peridotite, and gabbroic melt–peridotite, respectively. The background data represent bulk compositions of dolerite, oxide gabbro, gabbro, olivine gabbro, and troctolite from fore-arc region (Mortimer et al. 1998; Meffre et al. 2012; Falloon et al. 2014; Johnson et al. 2014), fast-spreading East Pacific Rise (EPR) (Pedersen et al. 1996; Natland and Dick 2009), slow-spreading Mid-Atlantic Ridge (MAR) (Godard et al. 2009), and ultraslow-spreading Southwest Indian Ridge (SWIR) (PetDB database: Lehnert et al. 2000). Compositional data of peridotites are from fore-arc region (Parkinson and Pearce 1998; Pearce et al. 2000; Birner et al. 2017), fast- to intermediate-spreading MOR (Niu and Hékinian 1997; Regelous et al. 2016; Niu 2004), slow-spreading MOR (Niu 2004; Regelous et al. 2016), and ultraslow-spreading MOR (Niu 2004; Regelous et al. 2016). Primitive upper mantle (PUM) data are from Jagoutz et al. (1979), Palme and Nickel (1985), Hart and Zindler (1986), and McDonough and Sun (1995). Abbreviations: Dol = dolerite, Du = dunite, Ga = gabbro, Ol ga = olivine gabbro, Ox ga = oxide gabbro, and Pe = peridotite

spreading center. Then, we discuss the origin of water in the magma and tectonic evolution (Sect. 7.6). We refer to Karson et al. (2015) for the classification of spreading rate as fast: 120–80 mm/year, intermediate: 80–50 mm/year, slow: 50–20 mm/year, and ultraslow: < 20 mm/year.

7.1 Magmatic evolution during the formation of Mado Megamullion 1: constraints from plutonic rocks

The gabbroic rocks from the Mado Megamullion are deformed to various degree from undeformed to mylonitic through porphyroclastic (Basch et al. 2020; Hirauchi et al. 2021). In places, they show lithological and structural contacts (Figs. 2d, 3e), which may correspond to tectonic contacts developed during detachment faulting (e.g., Harigane et al. 2011). Although they are tectonically disturbed to some degrees, numerous plutonic rocks were recovered from the Mado Megamullion (Table 1). This suggests the existence of active magmatism during the exhumation of Mado Megamullion. It is consistent with the numerical models that the detachment develops when appreciable amounts of
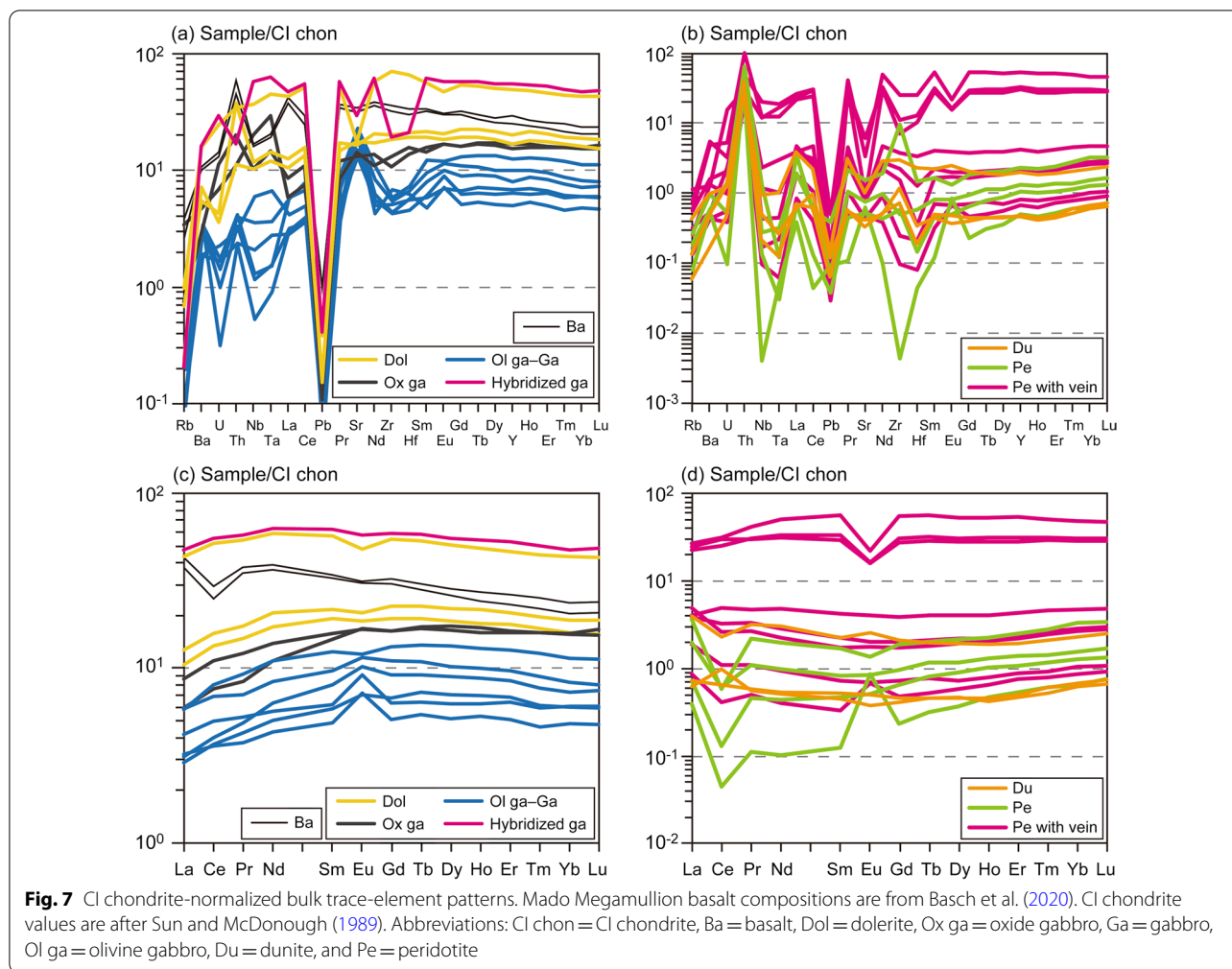
Fig. 6 Major-element mineral compositions (in wt%). Average data with 1 SD in **c**. The lines in **c** represent compositional trends defined by lower crustal rocks from fast-spreading EPR (pink), slow-spreading MAR (pale blue), and ultraslow-spreading SWIR (gray) by Basch et al. (2020). Amphibole classification in **d** is after Leake et al. (1997). Abbreviation: apfu = atoms per formula unit, Cpx = clinopyroxene, Dol = dolerite, Ga = gabbro, Ol ga = olivine gabbro, Ox ga = oxide gabbro, Pe = peridotite, and Pl = plagioclase

magma (30 to 50% of total plate separation) are present (Buck et al. 2005; Tucholke et al. 2008).

The gabbroic rocks show positive Eu and Sr anomalies in the CI chondrite-normalized trace-element patterns (Fig. 7a), suggesting the presence of cumulus plagioclase grains. In the view from MORB differentiation, typical tholeiitic evolution trend (e.g., Miyashiro 1974; Dick et al., 2002) is characterized by initial Fe-Ti enrichment followed by a Fe-Ti depletion with SiO_2 enrichment. The rationale behind the tholeiitic evolution trend is that the melts become saturated in Fe-Ti oxides at the kink point due to an increase of oxygen fugacity or water activity, leading to the oxide gabbro formation (e.g., Toplis and Carroll 1996; Botcharnikov et al. 2005; Koepke et al. 2018). Thus, the oxide gabbros in the Mado Megamullion formed from the highly differentiated late-stage ferrobasaltic magmas under an increased oxygen fugacity and/or

water activity at the final spreading stage of the Shikoku Basin. The kinks seen in the chemical trends from olivine gabbros/gabbros to oxide gabbros in Fig. 5a–c were probably emphasized by such magma differentiation process.

The magma differentiation is also corroborated from the presence of orthopyroxene in the olivine gabbros from the Mado Megamullion. The orthopyroxene grains are necessarily and intimately associated with the olivine grains in the olivine gabbros (Fig. 3c). This textural characteristic cannot be simply explained by the crystallization of an orthopyroxene-saturated melt at high-pressure or hydrous conditions (Berndt et al. 2005; Feig et al. 2006). Instead, we espouse a two-step peritectic reaction of olivine and evolved melt as described in detail by Zellmer et al. (2016): (1) the dissolution of Mg-rich olivine, which is rate-limited by Mg-Fe interdiffusion at the rim, and (2) the nucleation

Fig. 7 CI chondrite-normalized bulk trace-element patterns. Mado Megamullion basalt compositions are from Basch et al. (2020). CI chondrite values are after Sun and McDonough (1989). Abbreviations: CI chon = CI chondrite, Ba = basalt, Dol = dolerite, Ox ga = oxide gabbro, Ga = gabbro, Ol ga = olivine gabbro, Du = dunite, and Pe = peridotite

and growth of Mg-rich orthopyroxene preferentially in the melt boundary layer. Bloomer et al. (1991) reported a similar reaction process from the gabbros in the Atlantis Bank OCC in the SWIR, where the primitive lithologies such as olivine gabbros and troctolites are crosscut by evolved lithologies such as oxide gabbros and felsic rocks (Bloomer et al. 1991; Ozawa et al. 1991; Nguyen et al. 2018; Dick et al. 2019). It is thus plausible that the late, highly differentiated melt percolation through nearly solidified crystal framework caused the peritectic reactions to form orthopyroxene grains in the olivine gabbros. Similarly, the magmatic brown amphiboles are identified as granular or interstitial in almost all the igneous rocks from the Mado Megamullion (Fig. 3a–d; Table 1). As investigated more in detail in Sect. 7.6, the evolved melts were hydrous due to magma differentiation, and magmatic brown amphiboles were left along grain boundaries between anhydrous minerals as olivine, plagioclase, and clinopyroxene in the olivine gabbros (cf., Coogan et al. 2001).

In places, network-like vein intrusions of felsic rock crosscut the magmatic framework of gabbros in the Mado Megamullion, leaving hybridized gabbros (Basch et al. 2020). In terms of the modal proportion of brown amphibole, Fe-Ti oxide, and plagioclase, the felsic rocks are different in appearance; the brown amphibole and Fe-Ti oxide-rich mafic to felsic rocks show diffuse contacts with the host gabbros in comparison with the sharp contacts between the plagioclase-rich felsic rocks and the host gabbros (see Figure 5b and 5c in Basch et al. (2020)). Basch et al. (2020) demonstrated that the emplacement of the diffuse contact occurred at relatively higher temperatures up to ca. 850 °C than those of the sharp contact based on the detailed petrography and in-situ chemical analyses. Therefore, the parental melts of the network-like vein in the peridotites probably changed in chemical composition from mafic to felsic during the extensive cooling derived from the scarcity of melt supply and thus heat supply and/or hydrothermal fluid ingress along the detachment faults (Fig. 11a, b) (e.g., Coogan et al. 2007).
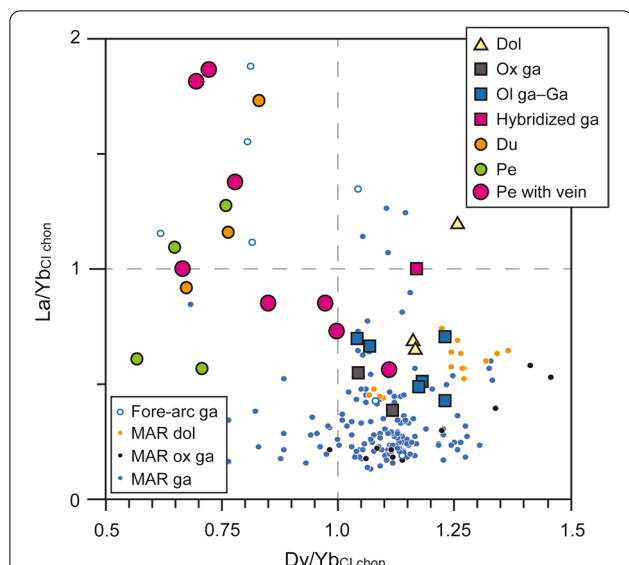
Fig. 8 Relationship between CI chondrite-normalized ratios of La/Yb and Dy/Yb. Compositional data from fore-arc region are after Meffre et al. (2012), Falloon et al. (2014) and Johnson et al. (2014). Those from slow-spreading MAR are after Godard et al. (2009). CI chondrite values are after Sun and McDonough (1989). Abbreviations: CI chon = CI chondrite, Dol = dolerite, Ox ga = oxide gabbro, Ga = gabbro, Ol ga = olivine gabbro, Du = dunite, and Pe = peridotite

An content–clinopyroxene Mg# space assuming that the primitive troctolites from the Godzilla Megamullion (Sanfilippo et al. 2013; 2016) can be a good candidate to represent primitive counterpart of the Mado Megamullion gabbros (the black broken arrow in Fig. 6c). On this basis, Basch et al. (2020) suggested that the steep decline from the fast-spreading EPR-like composition to ultraslow-spreading SWIR-like composition through the slow-spreading MAR-like composition, was due to a high-water content in the primary magmas. However, the magma genesis and magma differentiation process are possibly different between the Mado Megamullion and Godzilla Megamullion considering that the areal dimension of the former is significantly smaller ($\sim$ ca. 500 km^2) than the later ($\sim$ ca. 7000 km^2). Therefore, we indicate that the Godzilla Megamullion troctolites must be treated with peculiarity in terms of composition and cannot be directly related to the same crystalline descent that Basch et al. (2020) delineated for the Mado Megamullion (the black broken arrow in Fig. 6c). Excluding these Godzilla Megamullion troctolitic rocks, the intrinsic compositional trend of the Mado Megamullion in the plagioclase An content–clinopyroxene Mg# space rather mimics that of ultraslow-spreading SWIR (Fig. 6c). In summary, we favor a magma evolution process for the Mado Megamullion in which the water content was gradually concentrated through magma differentiation beneath the extinct spreading center in the Shikoku Basin. In this regard, the Mado Megamullion formed in a back-arc ridge analogous to the open ocean MOR. Further investigation and sample collection are desired in the Mado Megamullion to get primitive lithologies.
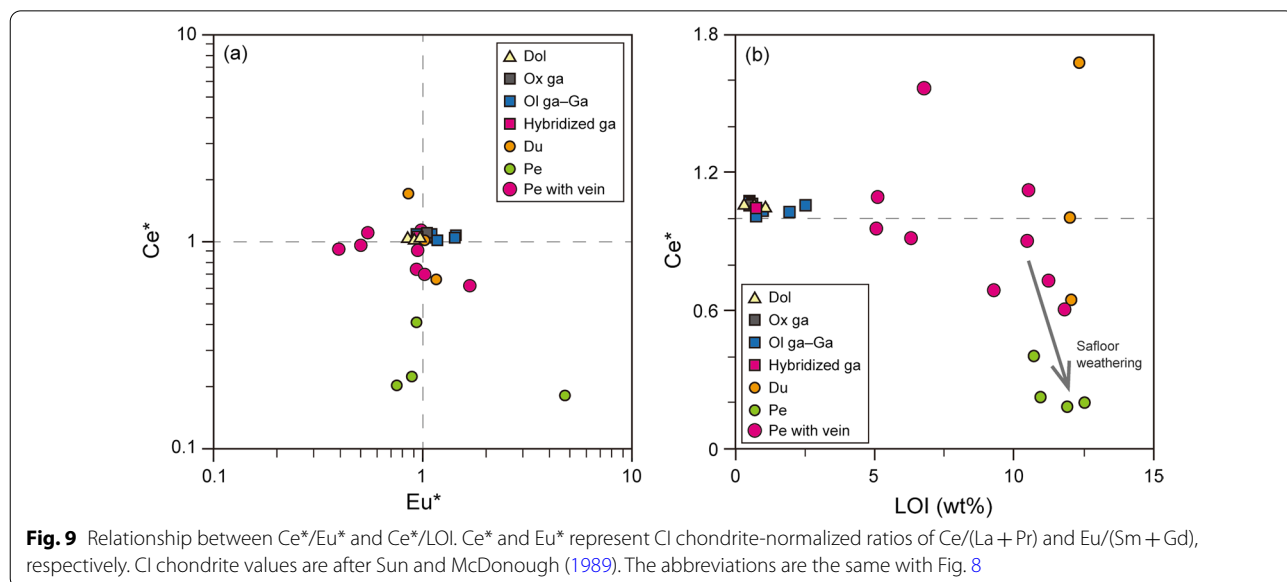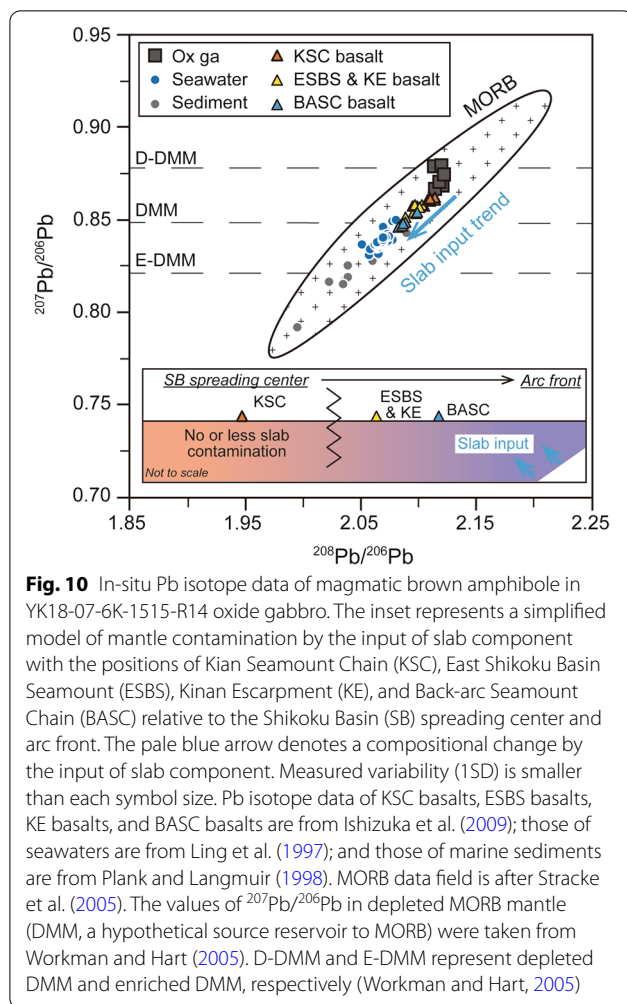
This hypothetical interpretation accords with the highly fractionated bulk chemical characteristics of the hybridized gabbro reported herein (Figs. 5, 7).

Although primitive lithologies such as troctolite have not been recovered from the Mado Megamullion, Basch et al. (2020) delineated a compositional trend particular to the Mado Megamullion in the plagioclase

Fig. 9 Relationship between Ce*/Eu* and Ce*/LOI. Ce* and Eu* represent CI chondrite-normalized ratios of Ce/(La + Pr) and Eu/(Sm + Gd), respectively. CI chondrite values are after Sun and McDonough (1989). The abbreviations are the same with Fig. 8

Fig. 10 In-situ Pb isotope data of magmatic brown amphibole in YK18-07-6K-1515-R14 oxide gabbro. The inset represents a simplified model of mantle contamination by the input of slab component with the positions of Kian Seamount Chain (KSC), East Shikoku Basin Seamount (ESBS), Kinan Escarpment (KE), and Back-arc Seamount Chain (BASC) relative to the Shikoku Basin (SB) spreading center and arc front. The pale blue arrow denotes a compositional change by the input of slab component. Measured variability (1SD) is smaller than each symbol size. Pb isotope data of KSC basalts, ESBS basalts, KE basalts, and BASC basalts are from Ishizuka et al. (2009); those of seawaters are from Ling et al. (1997); and those of marine sediments are from Plank and Langmuir (1998). MORB data field is after Stracke et al. (2005). The values of $^{207}Pb/^{206}Pb$ in depleted MORB mantle (DMM, a hypothetical source reservoir to MORB) were taken from Workman and Hart (2005). D-DMM and E-DMM represent depleted DMM and enriched DMM, respectively (Workman and Hart, 2005)

7.2 Magmatic evolution during the formation of Mado Megamullion 2: constraints from network-like veins in peridotites

The peridotites from the Mado Megamullion are crosscut by numerous network-like veins (Table 1), which range from gabbro to oxide gabbro in composition (Fig. 2e, f). Accordingly, the peridotite bulk major-element compositions show relative enrichments in gabbroic component (the pale blue arrows in Fig. 5a, b) or oxide gabbroic component (the black arrows in Fig. 5a, b), and the MREE/HREE ratios are higher in the peridotites associated with the network-like veins respect to the other peridotites (Figs. 7d, 8). Therefore, the peridotites are variously enriched as a result of elemental inputs derived from later intrusions of less evolved (gabbroic) to more evolved (oxide gabbroic) melts. This melt intrusion events were followed by partial replacement of pyroxenes by amphiboles (Fig. 3j). As demonstrated in detail by Natland and Dick (2001), these late melt intrusions and zone of deformation are intimately associated in the Atlantis

Bank OCC in the SWIR. The network-like veins and host gabbroic and peridotitic rocks record the crystal-plastic deformation evidenced by the occurrence of porphyroclasts with undulose extinction and kink bands with fine-grained neoblasts (Fig. 3i, l) (Basch et al. 2020; Hirauchi et al. 2021). All of the lines of evidence presented in Sects. 7.1 and 7.2 advocate that the vein network-forming melts percolated both into the plutonic and peridotitic rocks pervasively during the exhumation of the Mado Megamullion (Fig. 11b).

7.3 Magmatic evolution during the formation of Mado Megamullion 3: constraints from dunites

Dunites are widely reported from the seafloor and typically interpreted as fossilized melt channels (e.g., Warren 2016; Akizawa et al. 2020c). During the dunite channel formation by focused melt percolation, chromian spinels grow as a result of incongruent melting of orthopyroxenes (Nicolas and Prinzhofer 1983). We infer that the chromian spinels in the dunites from the Mado Megamullion were formed by infiltrating melt/peridotite reaction mechanism, as supported by the subhedral shape of the chromian spinels in the dunites (Fig. 3g), higher modal abundance of the chromian spinels in the dunites (2.6 to 6.4 vol%) respect to the peridotites (~ 1.9 vol%) (Table 1), and the close association between the chromian spinels and the orthopyroxenes (or bastite pseudomorphs after pyroxenes) in the dunites (Fig. 3g). We argue that SiO_2-poor melts generated by partial melting at higher pressures were focused and reacted with the peridotite at lower pressure (cf., Kelemen 1990; Akizawa et al. 2016). We outline a model in which the dunite formation predated later infiltrations of the gabbroic and oxide gabbroic veins as presented in Fig. 11a.

7.4 Mantle melting recorded in peridotites from Mado Megamullion

Abyssal peridotites are in general affected by seafloor weathering, causing substantial Mg loss (Snow and Dick 1995). The effect of seafloor weathering can be seen with the negative Ce anomalies in the CI chondrite-normalized trace-element patterns (Figs. 7d, 9b), inherited from the seawater composition (Niu 2004). Although we cannot eliminate elemental effects of seafloor weathering and melt infiltration, the Mado Megamullion peridotites without the network-like veins overlap the compositional range of the global abyssal peridotites from the slow- to ultraslow-spreading MOR in Mg/Si–Al/Si space (Fig. 5d).

Melting reactions in the spinel stability field (< ca. 2.5 GPa) produce olivine and liquid at the expense of pyroxenes and spinel along the peridotite solidus (e.g., Robinson et al. 1998). Residual peridotites are thereby enriched in Mg and depleted in Si and Al, forming an

Fig. 11 Schematic models for the evolution of Mado Megamullion. **a** Deep-seated formation of the dunites and gabbros. **b** Mafic to felsic melt intrusion during the progressive exhumation of the Mado Megamullion. **c** Dolerite dike intrusion at the final emplacement of the Mado Megamullion. **d** A concept of matured back-arc spreading during the formation of Mado Megamullion. Fertile mantle without subduction-related elemental input is the source of melt forming the Mado Megamullion. **a–c** were modified after Basch et al. (2020)

array with negative slope in Mg/Si and Al/Si space (cf. Pearson et al. 2003). The covariation of Mg/Si and Al/Si for a large data base of abyssal peridotites is plotted with chondritic meteorites in Fig. 5d. Considering the relative fertility in chemical composition (Fig. 5d) and in modal amount of pyroxenes and bastite pseudomorphs after pyroxenes (Table 1) of the Mado Megamullion peridotites studied here, we expect that they were originally lherzolites.

As explained in the introduction, some of the geochemical studies of BABB argued that high degrees of mantle melting are expected as a result of water introduction into the mantle source beneath the back-arc spreading center from the down-going slab (e.g., Stolper and Newman 1994; Taylor and Martinez 2003; Kelley et al. 2006). Although the introduction of water leads to a deepening of the melting regime down to the garnet stability field (Asimow and Langmuir 2003), there is in general

no garnet signature in BABB [cf. Langmuir et al. (2006) and references therein]. In principle, it is possible that the source mantle composition is significantly depleted and that garnet is no longer present, or that melting is not a fractional process so that melt remains in equilibrium with its residue and is extracted at shallow depths. Alternatively, Langmuir et al. (2006) developed a model of mixing between (1) melts produced by fractional melting of a water-poor source analogous to the depleted mantle typical at MOR, and (2) melts produced by equilibrium melting of a hydrous source receiving a high-water flux from the subducting slab and melted at shallow pressures. As we discussed in Sect. 7.1, the plutonic rocks from the Mado Megamullion are undistinguishable from those formed at slow- to ultraslow-spreading MOR. For this reason, we postulate that the contribution of water from the subducting slab was very limited or even negligible, and that the melting regime beneath the back-arc ridge was similar to those of an open ocean MOR during the formation of Mado Megamullion (Fig. 11d).

To estimate the melting extent of the Mado Megamullion peridotites, Yb concentration was used because they are much less mobile during late-stage events such as melt infiltration and weathering than the MREE and LREE (e.g., Yoshikawa and Nakamura 2000). The estimated melting extents of the Mado Megamullion peridotites roughly range between 3 and 15%, and were limited only within the spinel stability field (Fig. 12) (Sen et al. under review). Shallow mantle melting limited to the spinel stability field was also inferred from the bulk chemical composition of basalts from the post-spreading Kinan Seamount Chain (Ishizuka et al. 2009). Moreover, the Kinan Seamount Chain basalts show isotopic similarity to the MORB, with limited signatures of subduction-related elemental inputs (Ishizuka et al. 2009). Therefore, we can now infer that the magmas at the final spreading stage to the post-spreading stage of the Shikoku Basin were generated from a typical DMM without the subduction-related elemental input. This idea will be better substantiated in Sects. 7.5 and 7.6.

7.5 Post-spreading magmatism recorded in Mado Megamullion: constraints from dolerites

Few tens of centimeters-thick platy dolerite dikes could be traced over tens of meters in the massive Mado Megamullion peridotite body during DSV Shinkai 6500 submersible observation (Fig. 2b). The CI-chondrite-normalized REE patterns of dolerite are characterized by a steady decrease from MREE to LREE with flatness between MREE and HREE (Fig. 7c). The LREE-rich dolerite (YK18-07S-6K-1515-R11) exceptionally shows negative Eu and Sr anomalies (Fig. 7a, c), suggesting the crystallization from a melt that had experienced
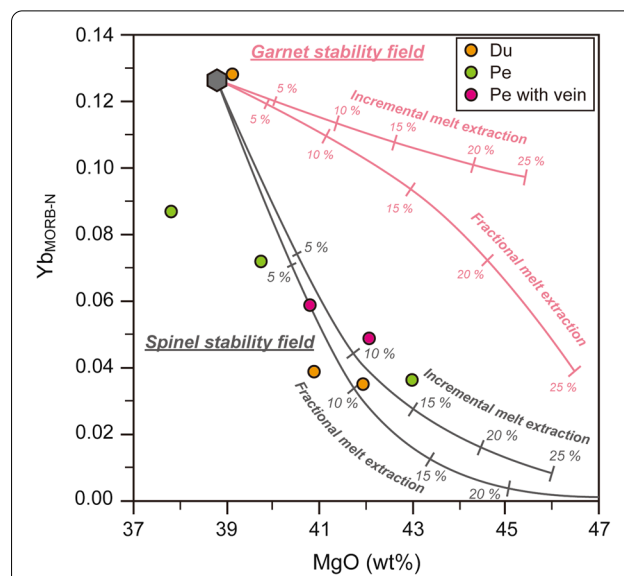
Fig. 12 Bulk compositional variation between MORB-normalized (MORB-N) Yb and MgO. Modeled melting trends during fractional and incremental batch melting of fertile mantle peridotite in the garnet stability field and spinel stability field are modified after Yoshikawa and Nakamura (2000). Abbreviations: Du = dunite, and Pe = peridotite

fractionation of plagioclase. In this regard, along with the compositional similarity (Figs. 5, 8), the dolerite-forming melts were variously fractionated and probably associated in part with the melt parental to the hybridized gabbro. However, we cannot fully predicate the genetic relationship of the dolerite and hybridized gabbro as assertive geological evidence and thorough isotopic perspective are lacking in the present status.

According to the thin-section observation, the dolerite dikes avoid the deformation associated with the exhumation of Mado Megamullion along the detachment faults. We thus suggest that variously fractionated melts intruded and formed the dolerite dike intrusions after the exhumation of Mado Megamullion at shallow depths (Fig. 11c). The spreading of Shikoku Basin ceased at ca. 15 Ma (Okino et al. 1994), but post-spreading volcanism associated with the formation of Kinan Seamount Chain lasted until ca. 7 Ma in the extinct back-arc spreading center (Ishizuka et al. 2009). The final vestiges of BAB magmatism probably lasted for several millions of years after the cessation of BAB spreading by residual mantle upwelling beneath the extinct back-arc spreading center (Ishizuka et al. 2009).

7.6 Origin of water and tectonic implication for evolution of Shikoku Basin

To a first approximation, BABB differ from MORB in magma genesis primarily because the enhanced water

content increases the degree of partial melting (e.g., Taylor and Martinez 2003; Kelley et al. 2006; Langmuir et al. 2006). Whereas melting regimes beneath the open ocean ridge system are considered to be roughly triangular in shape (e.g., Langmuir et al. 1992), those beneath BAB are considered to be asymmetric by both lateral mantle flow and water flux on the subduction side of the back-arc spreading ridge (Taylor and Martinez 2003; Langmuir et al. 2006). Mixing fertile mantle (upper mantle asthenosphere) with subduction component-bearing depleted mantle (hydrated mantle wedge) from the subduction side could be important where the back-arc spreading ridge and arc front converges. However, if the back-arc spreading ridge and arc front are well-separated, a subduction component is hardly added to the source mantle beneath the back-arc spreading ridge (Taylor and Martinez 2003; Kelley et al. 2006; Langmuir et al., 2006; Pearce and Stern 2006). Therefore, not only the present subduction system, but also the previous geometry of the back-arc spreading ridge, arc front, and down-going slab might affect the BABB composition. The combination of such temporal and spatial effects may tend to produce complex four-dimensional mixing of the source mantle beneath the BAB.

As for the present slab geometry beneath the Izu–Ogasawara–Mariana Trench, a number of data sources and seismic models have imaged that the subducting Pacific Plate is stagnated in the mantle transition zone beneath the southern Shikoku Basin, whereas the Pacific Plate seems to sink directly into the lower mantle beneath the Palace Vela Basin (e.g., Okino et al. 1989; Van der Hilst and Seno, 1993; Fukao et al., 2001; Li et al., 2008; Jaxybulatov et al., 2013). The numerical studies demonstrated that the buoyancy at the 660-km phase boundary acts as the obstructing force due to decomposition of ringwoodite with a negative Clapeyron slope (Fukao et al. (2009) and references therein), and facilitates stagnant slab formation, and following slab rollback and back-arc spreading (e.g., Tagawa et al. 2007; Nakakuki and Mura 2013). Although we cannot reconstruct time-dependent change of the slab geometry in the present study, our rock samples provide "a snapshot" in the final spreading stage of the Shikoku Basin, and can evaluate the effect of slab contamination to the source mantle using in-situ Pb isotope data set.

According to the in-situ Pb isotope analyses of the magmatic brown amphiboles in the oxide gabbro (Fig. 10), it is interpreted to have been crystallized from the melt originated from DMM that sourcing MORB at MOR, rather than from "slab-contaminated" mantle. The $^{207}Pb/^{206}Pb$ and $^{208}Pb/^{206}Pb$ data field of the magmatic

brown amphibole partly overlaps with that of Kinan Seamount Chain basalt, but distinct from those of basalts from East Shikoku Basin Seamount, Kinan Escarpment, and Back-arc Seamount Chain (Fig. 10). According to the perspectives from trace elements and multiple isotopes by Ishizuka et al. (2009), the basaltic magmas forming the Kinan Seamount Chain were generated from DMM without or slight slab contamination, whereas those forming the East Shikoku Basin Seamount, Kinan Escarpment, and Back-arc Seamount Chain were contaminated by the slab components. As simply outlined in the inset of Fig. 10, the Kinan Seamount Chain is most distant from the arc front among the above-listed localities. These chemical and geometrical characteristics lead us to indicate that the negative trend toward the seawaters and sediments in the $^{207}Pb/^{206}Pb$ and $^{208}Pb/^{206}Pb$ space is "slab input trend" (Fig. 10), and the magmatic water stored in the magmatic brown amphiboles in the oxide gabbro (Figs. 3b, 4) was derived solely from an asthenospheric mantle that sourcing MORB at MOR. The Shikoku Basin was probably well apart from the subducting slab, due to for example the slab stagnation accompanied by the slab rollback and back-arc spreading through the maturing of Shikoku Basin (Fig. 11d).

The magmatic brown amphiboles and clinopyroxenes are often replaced by green to pale brown amphiboles (Figs. 3d, 3e, 4). The replacement boundaries are wavy and gradual in chemical composition (Fig. 4). Harigane et al. (2019) investigated the green amphiboles in close association with the magmatic brown amphiboles in the gabbros from the Godzilla Megamullion, and demonstrated that retrograde metamorphic reactions with introduction of seawater-derived fluids were necessary to form the green amphiboles (cf., Harigane et al. 2010, 2011). The color, thus compositional variations of the amphiboles from pargasite to tremolite through edenite and hornblend (Fig. 6d) are attributed to the multiple origin under magmatic to metamorphic conditions.

8 Conclusions

We presented bulk and in-situ chemical compositions with in-situ Pb isotope composition of dolerite, oxide gabbro, gabbro, olivine gabbro, dunite, and peridotite collected at the Mado Megamullion, Shikoku Basin. The rock samples recovered from the Mado Megamullion are similar in lithology and chemical composition with those from the slow- to ultraslow-spreading MOR. We outline a possible magmatic and tectonic story that the Mado Megamullion had recorded at the final spreading stage of Shikoku Basin.

The mantle started melting in the spinel stability field to generate BABB beneath the back-arc spreading center. The melts generated at deeper depths were focused forming channelized dunite at shallower depths. The mechanism of dunite formation was incongruent melting of orthopyroxene in the former peridotite, induced by the input of SiO_2-poor melt generated at high pressures in the spinel stability field. The magmas were highly evolved to hydrous, ferrobasaltic composition, and precipitated magmatic brown amphiboles and Fe-Ti oxides. Cutting off from fresh magma replenishment eventually functioned to highly differentiate the magmas. Since the timing of the exhumation of Mado Megamullion corresponds to the very end of the spreading of Shikoku Basin, the magma supply was subdued and highly episodic beneath the back-arc spreading center, which is analogous to the slow- to ultraslow-spreading MOR. The evolved melts later intruded pervasively into the plutonic and peridotitic rocks along the detachment faults during the exhumation of Mado Megamullion to form network-like mafic to felsic veins. Afterward, seawater-derived fluid inputs occurred along the detachment faults, and locally modified the pristine magmatic assemblages with forming green amphiboles as a product of retrograde metamorphic reaction.

The distance from the back-arc spreading center to the arc front increased away through maturing of Shikoku Basin. Since the back-arc spreading ridge and arc front were well-separated, the subduction component could not be added to the source mantle beneath the back-arc spreading center. The dolerite intrusion postdated the exhumation of Mado Megamullion. In the Shikoku Basin, post-spreading volcanism, called Kinan Seamount Chain, overlaps in the extinct back-arc spreading center. The spreading of the Shikoku Basin terminated at ca. 15 Ma, whereas the post-spreading volcanism lasted up to ~7 Ma. The magma injections had continued from the final spreading stage to the post-spreading stage of the Shikoku Basin for several millions of years by residual mantle upwelling beneath the extinct back-arc spreading center. Time-dependent geometry of the back-arc spreading center, arc front, and down-going slab probably affect the BABB composition. The combination of such temporal and spatial effects may tend to produce complex four-dimensional mixing of the source mantle beneath the BAB. The Mado Megamullion is of profound importance to investigate the slow- to ultraslow-spreading MOR-like magmatic and tectonic history at the final spreading stage of the Shikoku Basin.

Abbreviations
BAB: Back-arc basin; BABB: Back-arc basin basalt; HFSE: High field strength element; IAB: Island-arc basalt; LILE: Large ion lithophile element; MOR: Mid-ocean ridge; MORB: Mid-ocean ridge basalt; OCC: Oceanic core complex.

Supplementary Information
The online version contains supplementary material available at https://doi.org/10.1186/s40645-021-00454-3.

Additional file 1. The instrumentation, analytical settings and analytical datasets supporting the conclusions of this article are all included within the article as Tables S1 to S12.

Authors' contributions
KO and YO designed the cruise expeditions. NA designed this study using the rock samples collected during the expeditions. NA, HY, and SM prepared sample powders. NA, and OI carried out the bulk chemical analyses. NA, HA, and TH analyzed in-situ Pb isotope composition of the amphiboles. NA, YO, KO, OI, HY, SM, AS, VB, JS, AS, YH, KH, KM, MF, and HA contributed to construct the geological interpretation in this study. All authors read and approved the final manuscript.

Availability of data and materials
The datasets are all included in the article.

Declarations

Competing interests
The authors declare that they have no competing interest.

Author details
[1]Atmosphere and Ocean Research Institute, The University of Tokyo, 5-1-5 Kashiwanoha, Kashiwa, Chiba 277-8564, Japan. [2]Hydrographic and Oceanographic Department of Japan, 3-1-1 Kasumigaseki, Chiyoda, Tokyo 100-8932, Japan. [3]Japan Agency for Marine-Earth Science and Technology, 2-15 Natsushima, Yokosuka, Kanagawa 237-0061, Japan. [4]Department of Earth and Planetary Sciences, Nagoya University, Furocho, Chikusa, Nagoya 464-8601, Japan. [5]Research Institute of Earthquake and Volcano Geology, National Institute of Advanced Industrial Science and Technology, 1-1-1 Higashi, Tsukuba, Ibaraki 305-8567, Japan. [6]Kanagawa Prefectural Museum of Natural History, 499 Iryuda, Odawara, Kanagawa 250-0031, Japan. [7]Ocean Resources Research Center for Next Generation, Chiba Institute of Technology, 2-17-1 Tsudanuma, Narashino, Chiba 275-0016, Japan. [8]Dipartimento di Scienze della Terra e dell'ambiente, University of Pavia, 1 Via Ferrata, Pavia, Italy. [9]Department of Geology and Geophysics, Louisiana State University, Baton Rouge, LA 70803, USA. [10]Department of Earth and Atmospheric Sciences, University of Houston, Houston, TX 77204, USA. [11]Department of Geosciences, Shizuoka University, 836 Ohya, Suruga, Shizuoka 422-8529, Japan. [12]National Institute of Polar Research/SOKENDAI, Tachikawa, Tokyo 190-8518, Japan. [13]Geochemical Research Center, The University of Tokyo, 7-3-1 Hongo, Bunkyo, Tokyo 113-0033, Japan.

Akizawa *et al. Progress in Earth and Planetary Science*   (2021) 8:65

Page 21 of 24

References

Akizawa N, Okino K, Ishizuka O, Yamashita H, Fujii M, Ohara Y (2020a) Petrological and geophysical implications for Mado Megamullion. Latest Earth 1:57–61. https://sites.google.com/view/mantlepress/home. Accessed 18 June 2021

Akizawa N, Ishikawa A, Kogiso T (2020b) A simple determination of whole-rock major- and trace-element composition for peridotite by micro-XRF spectrometer and ICP-MS using fused-glass bead. Geochem J 54:81–90. https://doi.org/10.2343/geochemj.2.0587

Akizawa N, Früh-Green G, Tamura A, Tamura C, Morishita T (2020c) Compositional heterogeneity and melt transport in mantle beneath Mid-Atlantic Ridge constrained by peridotite, dunite, and wehrlite from Atlantis Massif. Lithos 354–355:105364. https://doi.org/10.1016/j.lithos.2019.105364

Akizawa N, Ozawa K, Tamura A, Michibayashi K, Arai S (2016) Three-dimensional evolution of melting, heat and melt transfer in ascending mantle beneath a fast-spreading ridge segment constrained by trace elements in clinopyroxene from concordant dunites and host harzburgites of the Oman ophiolite. J Petrol 57:777–814. https://doi.org/10.1093/petrology/egw020

Arai R, Dunn RA (2014) Seismological study of Lau back arc crust: mantle water, magmatic differentiation, and a compositionally zoned basin. Earth Planet Sci Lett 390:304–317. https://doi.org/10.1016/j.epsl.2014.01.014

Asimow PD, Langmuir CH (2003) The importance of water to oceanic mantle melting regimes. Nature 421:815–820. https://doi.org/10.1038/nature01429

Basch V, Sanfilippo A, Sani C, Ohara Y, Snow J, Ishizuka O, Harigane Y, Michibayashi K, Sen A, Akizawa N, Okino K, Fujii M, Yamashita H (2020) Crustal accretion in a slow spreading back-arc basin: Insights from the Mado Megamullion Oceanic Core Complex in the Shikoku Basin. Geochem Geophys Geosyst 21:e2020GC009199. https://doi.org/10.1029/2020GC009199

Berndt J, Koepke J, Holtz F (2005) An experimental investigation of the influence of water and oxygen fugacity on differentiation of MORB at 200 MPa. J Petrol 46:135–167. https://doi.org/10.1093/petrology/egh066

Birner SK, Warren JM, Cottrell E, Davis FA, Kelley KA, Falloon TJ (2017) Forearc peridotites from Tonga record heterogeneous oxidation of the mantle following subduction initiation. J Petrol 58:1755–1779. https://doi.org/10.1093/petrology/egx054

Bloomer SH, Meyer PS, Dick HJB, Ozawa K, Natland JH (1991) Textural and mineralogic variations in gabbroic rocks from Hole 735B. In: Von Herzen RP, Robinson PT et al (eds) Proc ODP, Sci Results 118. College Station, TX, pp 21–36

Botcharnikov RE, Koepke J, Holtz F, McCammon C, Wilke M (2005) The effect of water activity on the oxidation and structural state of Fe in a ferrobasaltic melt. Geochim Cosmochim Acta 69:5071–5085. https://doi.org/10.1016/j.gca.2005.04.023

Buck WR, Lavier LL, Poliakov ANB (2005) Models of faulting at mid-ocean ridges. Nature 434:719–723. https://doi.org/10.1038/nature03358

Cann JR, Blackman DK, Smith DK, Mcallister E, Janssen B, Mello S, Avgerinos E, Pascoe AR, Escartin J (1997) Corrugated slip surfaces formed at ridge-transform intersections o the Mid-Atlantic Ridge. Nature 385:329–332. https://doi.org/10.1038/385329a0

Coogan LA, Manning CE, Wilson RN, EIMF (2007) Oxygen isotope evidence for short-lived high-temperature fluid flow in the lower oceanic crust at fast-spreading ridges. Earth Planet Sci Lett 260:524–536. https://doi.org/10.1016/j.epsl.2007.06.013

Coogan LA, Wilson RN, Gillis KM, MacLeod CJ (2001) Near-solidus evolution of oceanic gabbros: insights from amphibole geochemistry. Geochim Cosmochim Acta 65:4339–4357. https://doi.org/10.1016/S0016-7037(01)00714-1

Dick HJB, Kvassnes AJS, Robinson PT, MacLeod CJ, Kinoshita H (2019) The Atlantis Bank gabbro massif, Southwest Indian Ridge. Prog Earth Planet Sci 6:64. https://doi.org/10.1186/s40645-019-0307-9

Dick HJB, Ozawa K, Meyer PS, Niu Y, Robinson PT, Constantin M, Hebert R,Maeda J, Natland JH, Gregory H, Mackie SM (2002) Primary silicate mineral chemistry of a 1.5-km section of very slow spreading lower ocean crust: ODP Hole 753B, Southwest Indian Ridge. In: Natland JH, Dick HJB et al. (eds), Proc ODP, Sci Results 176. College Station, TX, pp 1–61

Eason DE, Dunn RA (2015) Petrogenesis and structure of oceanic crust in the Lau back-arc basin. Earth Planet Sci Lett 429:128–138. https://doi.org/10.1016/j.epsl.2015.07.065

Eggins SM, Kinsley LPJ, Shelley JMG (1998) Deposition and element fractionation processes during atmospheric pressure laser sampling for analysis by ICP-MS. Appl Surf Sci 127–129:278–286. https://doi.org/10.1016/S0169-4332(97)00643-0

Elburg M, Vroon P, van der Wagt B, Tchalikian A (2005) Sr and Pb isotopic composition of five USGS glasses (BHVO-2G, BIR-1G, BCR-2G, TB-1G, NKT-1G). Chem Geol 223:196–207. https://doi.org/10.1016/j.chemgeo.2005.07.001

Falloon TJ, Meffre S, Crawford AJ, Hoernle K, Hauff F, Bloomer SH, Wright DJ (2014) Cretaceous fore-arc basalts from the Tonga arc: geochemistry and implications for the tectonic history of the SW Pacific. Tectonophysics 630:21–32. https://doi.org/10.1016/j.tecto.2014.05.007

Feig S, Koepke J, Snow J (2006) Effect of water on tholeiitic basalt phase equilibria: an experimental study under oxidizing conditions. Contrib Mineral Petrol 152:611–638. https://doi.org/10.1007/s00410-006-0123-2

Fukao Y, Widiyantoro S, Obayashi M (2001) Stagnant slabs in the upper and lower mantle transition region. Rev Geophys 39:291–323. https://doi.org/10.1029/1999RG000068

Fukao Y, Obayashi M, Nakakuki T, the Deep Slab Project Group (2009) Stagnant slab: a review. Annu Rev Earth Planet Sci 37:19–46. https://doi.org/10.1146/annurev.earth.36.031207.124224

Gill JB (1976) Composition and age of Lau Basin and Ridge volcanic rocks: implications for evolution of an interarc basin and remnant arc. Geol Soc Am Bull 87:1384–1395. https://doi.org/10.1130/0016-7606(1976)87%3c1384:CAAOLB%3e2.0.CO;2

Gladney ES, Roelandts I (1988a) 1987 compilation of elemental concentration data for USGS BIR-1, DNC-1 and W-2. Geostand Newsl 12:63–118. https://doi.org/10.1111/j.1751-908X.1988.tb00044.x

Gladney ES, Roelandts I (1988b) 1987 compilation of elemental concentration data for USGS BHVO-1, MAG-1, QLO-1, RGM-1, SCo-1, SDC-1, SGR-1 and STM-1. Geostand Newsl 12:253–362. https://doi.org/10.1111/j.1751-908X.1988.tb00053.x

Godard M, Awaji S, Hansen H, Hellebrand E, Brunelli D, Johnson K, Yamasaki T, Maeda J, Abratis M, Christie D, Kato Y, Mariet C, Rosner M (2009) Geochemistry of a long in-situ section of intrusive slow-spread oceanic lithosphere: results from IODP Site U1309 (Atlantis Massif, 30°N Mid-Atlantic-Ridge). Earth Planet Sci Lett 279:110–122. https://doi.org/10.1016/j.epsl.2008.12.034

Günther D, Heinrich CA (1999) Enhanced sensitivity in laser ablation-ICP mass spectrometry using helium–argon mixtures as aerosol carrier. J Anal at Spectrom 14:1363–1368. https://doi.org/10.1039/A901648A

Harigane Y, Okamoto A, Morishita T, Snow JE, Tamura A, Yamashita H, Michibayashi K, Ohara Y, Arai S (2019) Melt-fluid infiltration along detachment shear zones in oceanic core complexes: Insights from amphiboles in gabbro mylonites from the Godzilla Megamullion, Parece Vela Basin, the Philippine Sea. Lithos 344–345:217–231. https://doi.org/10.1016/j.lithos.2019.06.019

Harigane Y, Michibayashi K, Ohara Y (2011) Deformation and hydrothermal metamorphism of gabbroic rocks within the Godzilla Megamullion, Parece Vela Basin, Philippine Sea. Lithos 124:185–199. https://doi.org/10.1016/j.lithos.2011.02.001

Harigane Y, Michibayashi K, Ohara Y (2010) Amphibolitizationwithin the lower crust in the termination area of the Godzilla Megamullion, Parece Vela backarc basin. Isl Arc 19:718–730. https://doi.org/10.1111/j.1440-1738.2010.00741.x

Hart SR, Zindler A (1986) In search of a bulk Earth composition. Chem Geol 57:247–267. https://doi.org/10.1016/0009-2541(86)90053-7

Hawkins JW, Melchior JT (1985) Petrology of Mariana Trough and Lau Basin basalts. J Geophys Res 90:11431–11468. https://doi.org/10.1029/JB090iB13p11431

Hickey-Vargas R (1991) Isotope characteristics of submarine lavas from the Philippine Sea: implications for the origin of arc and basin magmas of the Philippine tectonic plate. Earth Planet Sci Lett 107:290–304. https://doi.org/10.1016/0012-821X(91)90077-U

Hirauchi K-I, Segawa I, Kouketsu Y, Harigane Y, Ohara Y, Snow J, Sen A, Fujii M, Okino K (2021) Alteration processes recorded by back-arc mantle peridotites from oceanic core complexes, Shikoku Basin. Philippine Sea Isl Arc 30:e12419. https://doi.org/10.1111/iar.12419

Hirschmann MM, Asimow PD, Ghiorso MS, Stolper EM (1999) Calculation of peridotite partial melting from thermodynamic models of minerals and melts. III. Controls on isobaric melt production and the effect of water on melt production. J Petrol 40:831–851. https://doi.org/10.1093/petroj/40.5.831

Ikeda Y, Nagao K, Stern RJ, Yuasa M, Newman S (1998) Noble gases in pillow basalt glasses from the northern Mariana Trough back-arc basin. Isl Arc 7:471–478. https://doi.org/10.1111/j.1440-1738.1998.00204.x

Imai N, Terashima S, Itoh S, Ando A (1995) 1994 compilation values for GSJ reference samples, "Igneous rock series." Geochem J 29:91–95. https://doi.org/10.2343/geochemj.29.91

Imai N, Terashima S, Itoh S, Ando A (1996) 1996 compilation of analytical data on nine GSJ geochemical reference samples, "Sedimentary rock series." Geostand Newsl 20:165–216. https://doi.org/10.1111/j.1751-908X.1996.tb00184.x

Imai N, Terashima S, Itoh S, Ando A (1999) 1998 compilation of analytical data for five GSJ geochemical reference samples: The "Instrumental analysis series." Geostand Newsl 23:223–250. https://doi.org/10.1111/j.1751-908X.1999.tb00576.x

Ishizuka O, Taylor RN, Umino S, Kanayama K (2020) Geochemical evolution of arc and slab following subduction initiation: a record from the Bonin Islands, Japna. J Petrol 61:egaa050. https://doi.org/10.1093/petrology/egaa050

Ishizuka O, Taylor RN, Yuasa M, Ohara Y (2011) Making and breaking an island arc: a new perspective from the Oligocene Kyushu-Palau arc, Philippine Sea. Geochem Geophys Geosyst 12:Q05005. https://doi.org/10.1029/2010GC003

Ishizuka O, Yuasa M, Taylor RN, Sakamoto I (2009) Two contrasting magmatic types coexist after the cessation of back-arc spreading. Chem Geol 266:274–296. https://doi.org/10.1016/j.chemgeo.2009.06.014

Jagoutz E, Palme H, Baddenhausen H, Blum K, Cendales M, Dreibus G, Spettel B, Lorenz V, Wanke H (1979) The abundances of major, minor and trace elements in the Earth's mantle as derived from primitive ultramafic nodules. Lunar Planet Sci Conf 10:2031–2050

Jaxybulatov K, Koulakov I, Dobretsov NL (2013) Segmentation of the Izu-Bonin and Mariana slabs based on the analysis of the Benioff seismicity distribution and regional tomography results. Solid Earth 4:59–73. https://doi.org/10.5194/se-4-59-2013

Jochum KP, Weis U, Schwager B, Stoll B, Wilson SA, Haug GH, Andreae MO, Enzweiler J (2016) Reference values following ISO guidelines for frequently requested rock reference materials. Geostand Geoanalytical Res 40:333–350. https://doi.org/10.1111/j.1751-908X.2015.00392.x

Johnson JA, Hickey-Vargas R, Fryer P, Salters V, Reagan M (2014) Geochemical and isotopic study of a plutonic suite and related early volcanic sequences in the southern Mariana forearc. Geochem Geophys Geosyst 15:589–604. https://doi.org/10.1002/2013GC005053

Karson JA, Kelley DS, Fornari DJ, Perfit MR, Shank TM (2015) Discovering the deep: a photographic atlas of the seafloor and ocean crust. Cambridge University Press, Cambridge

Kelemen PB (1990) Reaction between ultramafic rock and fractionating basaltic magma I. Phase relations, the origin of calc-alkaline magma series, and the formation of discordant dunite. J Petrol 31:51–98. https://doi.org/10.1093/petrology/31.1.51

Kelley KA, Plank T, Grove TL, Stolper EM, Newman S, Hauri E (2006) Mantle melting as a function of water content beneath back-arc basins. J Geophys Res 111:B09208. https://doi.org/10.1029/2005JB003732

Kendrick MA, Danyushevsky LV, Falloon TJ, Woodhead JD, Arculus RJ, Ireland T (2020) SW Pacific arc and backarc lavas and the role of slab-bend serpentinites in the global halogen cycle. Earth Planet Sci Lett 530:115921. https://doi.org/10.1016/j.epsl.2019.115921

Kimura J-I, Chang Q, Kanazawa N, Sasaki S, Vaglarov BS (2016) High-precision in situ analysis of Pb isotopes in glasses using $10^{13}\Omega$ resistor high gain amplifiers with ultraviolet femtosecond laser ablation multiple Faraday collector inductively coupled plasma mass spectrometry. J Anal at Spectrom 31:790–800. https://doi.org/10.1039/c5ja00374a

Koepke J, Botcharnikov RE, Natland JH (2018) Crystallization of late-stage MORB under varying water activities and redox conditions: implications for the formation of highly evolved lavas and oxide gabbro in the ocean crust. Lithos 323:58–77. https://doi.org/10.1016/j.lithos.2018.10.001

Koepke J, France L, Müller T, Faure F, Goetze N, Dziony W, Ildefonse B (2011) Gabbros from IODP Site 1256, equatorial Pacific: Insight into axial magma chamber processes at fast spreading ocean ridges. Geochem Geophys Geosyst 12:Q09014. https://doi.org/10.1029/2011GC003655

Langmuir CH, Bézos A, Escrig S, Parman SW (2006) Chemical systematics and hydrous melting of the mantle in back-arc basins. In: Christie DM, Fisher CR, Lee S-M, Givens S (eds) Back-arc spreading systems: geological, biological, chemical, and physical interactions. Geophys Monogr Ser 166. AGU, Washington DC, pp 87–146

Langmuir CH, Klein EM, Planck T (1992) Petrological systematics of mid-ocean ridge basalts: Constraints on melt generation beneath ocean ridges. In: Morgan JP, Blackman DK, Sinton JM (eds) Mantle flow and melt generation at Mid-Ocean Ridges. AGU, Washington, pp 183–280

Leake BE, Woolley AR, Arps CES, Birch WD, Gilbert MC, Grice JD, Hawthorne FC, Kato A, Kisch HJ, Krivovichev VG, Linthout K, Laird J, Mandrino J, Maresch WV, Nickel EH, Rock NMS, Schumacher JC, Smith DC, Stephenson NCN, Ungaretti L, Whittaker EJW, Youzhi G (1997) Nomenclature of amphiboles: report of the subcommittee on amphiboles of the international mineralogical association commission on new minerals and mineral names. Can Mineral 35:219–246. https://doi.org/10.1180/minmag.1997.061.405.13

Lehnert K, Su Y, Langmuir CH, Sarbas B, Nohl U (2000) A global geochemical database structure for rocks. Geochem Geophys Geosyst 1:1012. https://doi.org/10.1029/1999GC000026

Li C, van der Hilst RD, Engdahl ER, Burdick S (2008) A new global model for P wave speed variations in Earth's mantle. Geochem Geophys Geosys 9:Q05018. https://doi.org/10.1029/2007GC001806

Ling HF, Burton KW, O'Nions RK, Kamber BS, von Blanckenburg F, Gibb AJ, Hein JR (1997) Evolution of Nd and Pb isotopes in Central Pacific seawater from ferromanganese crusts. Earth Planet Sci Lett 146:1–12. https://doi.org/10.1016/S0012-821X(96)00224-5

Loocke M, Snow JE, Ohara Y (2013) Melt stagnation in peridotites from the Godzilla Megamullion Oceanic Core Complex, Parece Vela Basin, Philippine Sea. Lithos 182–183:1–10. https://doi.org/10.1016/j.lithos.2013.09.005

Makino Y, Kuroki Y, Hirata T (2019) Determination of major to trace elements in metallic materials based on the solid mixing calibration method using multiple spot-laser ablation-ICP-MS. J Anal at Spectrom 34:1794–1799. https://doi.org/10.1039/C9JA00181F

McDonough WF, Sun SS (1995) The composition of the earth. Chem Geol 120:223–253. https://doi.org/10.1016/0009-2541(94)00140-4

Meffre S, Falloon TJ, Crawford TJ, Hoernle K, Hauff F, Duncan RA, Bloomer SH, Wright DJ (2012) Basalts erupted along the Tongan fore arc during subduction initiation: Evidence from geochronology of dredged rocks from the Tonga fore arc and trench. Geochem Geophys Geosyst 13:Q12003. https://doi.org/10.1029/2012GC004335

Miyashiro A (1974) Volcanic rock series in island arcs and active continental margins. Am J Sci 274:321–355

Mortimer N, Herzer RH, Gans PB, Parkinson DL, Seward D (1998) Basement geology from Three Kings Ridge to West Norfolk Ridge, southwest Pacific Ocean: evidence from petrology, geochemistry and isotopic dating of dredge samples. Mar Geol 148:135–162. https://doi.org/10.1016/S0025-3227(98)00007-3

Nakakuki T, Mura E (2013) Dynamics of slab rollback and induced back-arc basin formation. Earth Plane Sci Lett 361:287–297. https://doi.org/10.1016/j.epsl.2012.10.031

Natland JH, Dick HJB (2009) Paired melt lenses at the East Pacific Rise and the pattern of melt flow through the gabbroic layer at a fast-spreading ridge. Lithos 112:73–86. https://doi.org/10.1016/j.lithos.2009.06.017

Natland JH, Dick HJB (2001) Formation of the lower ocean crust and the crystallization of gabbroic cumulates at a very slow spreading ridge. J Volcanol Geotherm Res 110:191–233. https://doi.org/10.1016/S0377-0273(01)00211-6

Nguyen DK, Morishita T, Soda Y, Tamura A, Ghosh B, Harigane Y, France L, Liu C, Natland JH, Sanfilippo A, MacLeod CJ, Blum P, Dick HJB (2018) Occurrence of felsic rocks in oceanic gabbros from IODP Hole U1473A: Implications for evolved melt migration in the lower oceanic crust. Minerals 8:583. https://doi.org/10.3390/min8120583

Nicolas A, Prinzhofer A (1983) Cumulative or residual origin for the transition zone in ophiolites: structural evidence. J Petrol 24:188–206. https://doi.org/10.1093/petrology/24.2.188

Niu Y (2004) Bulk-rock major and trace element compositions of abyssal peridotites: implications for mantle melting, melt extraction and post-melting processes beneath mid-ocean ridges. J Petrol 45:2423–2458. https://doi.org/10.1093/petrology/egh068

Niu Y, Hékinian R (1997) Basaltic liquids and harzburgitic residues in the Garrett Transform: a case study at fast-spreading ridges. Earth Planet Sci Lett 146:43–258. https://doi.org/10.1016/S0012-821X(96)00218-X

Ohara Y, Okino K, Akizawa N, Fujii M, Harigane Y, Hirano N, Hirauchi K-I, Machida S, Michibayashi K, Sanfilippo A, Snow JE, Yamashita H (2018) A new tectonic window into the backarc basin lower oceanic crust and upper mantle: Mado Megamullion in the Shikoku Basin. AGU Fall Meeting, T32C-05B

Ohara Y, Fujioka K, Ishii T, Yurimoto H (2003) Peridotites and gabbros from the Parece Vela backarc basin: unique tectonic window in an extinct backarc spreading ridge. Geochem Geophys Geosyst 4:8611. https://doi.org/10.1029/2002GC000469

Ohara Y, Stern RJ, Ishii T, Yurimoto H, Yamazaki T (2002) Peridotites from the Mariana Trough: first look at the mantle beneath an active back-arc basin. Contrib Mineral Petrol 143:1–18. https://doi.org/10.1007/s00410-001-0329-2

Ohara Y, Yoshida T, Kato Y, Kasuga S (2001) Giant Megamullion in the Parece Vela Backarc basin. Mar Geophys Res 22:47–61. https://doi.org/10.1023/A:1004818225642

Okino K, Ohara Y, Fujii M, Hanyu T (2019) Evolution of oceanic core complexes in the Shikoku Basin: When backarc basins cease to open. Japan Geoscience Union Meeting, SCG56-P06

Okino K (2015) Magnetic anomalies in the Philippine Sea: implications for regional tectonics. J Geogr 124:729–747. https://doi.org/10.5026/jgeography.124.729 (**in Japanese with English abstract**)

Okino K, Ohara Y, Kasuga S, Kato Y (1999) The Philippine Sea: New survey results reveal the structure and the history of the marginal basin. Geophys Res Lett 26:2287–2290. https://doi.org/10.1029/1999GL900537

Okino K, Kasuga S, Ohara Y (1998) A new scenario of the Parece Vela basin genesis. Mar Geophys Res 20:21–40. https://doi.org/10.1023/A:1004377422118

Okino K, Shimakawa Y, Nagaoka S (1994) Evolution of the Shikoku basin. J Geomag Geoelectr 46:463–479. https://doi.org/10.5636/jgg.46.463

Okino K, Ando M, Kaneshima S, Hirahara K (1989) The horizontally lying slab. Geophys Res Lett 16:1059–2062. https://doi.org/10.1029/GL016i009p01059

Ozawa K, Meyer PS, Bloomer SH (1991) Mineralogy and textures of iron-titanium-oxide gabbros from hole 735B. In: Von Herzen RP, Robinson PT et al (eds) Proc ODP, Sci Results 118. College Station, TX, pp 41–73

Palme H, Nickel K (1985) Ca/Al ratio and composition of the Earth's mantle. Geochim Cosmochim Acta 49:2123–2132. https://doi.org/10.1016/0016-7037(85)90070-5

Parkinson IJ, Pearce JA (1998) Peridotites from the Izu–Bonin–Mariana forearc (ODP Leg 125): evidence for mantle melting and melt–mantle interaction in a supra-subduction zone setting. J Petrol 39:1577–1618. https://doi.org/10.1093/petroj/39.9.1577

Parman SW, Grove TL (2004) Harzburgite melting with and without H_2O: experimental data and predictive modeling. J Geophys Res 109:B02201. https://doi.org/10.1029/2003JB002566

Pearce JA, Stern RJ (2006) Origin of back-arc basin magmas: trace element and isotope perspectives. In: Christie DM, Fisher CR, Lee S-M, Givens S (eds) Back-arc spreading systems: geological, biological, chemical, and physical interactions. Geophys Monogr Ser 166. AGU, pp 63–86

Pearce JA, Barker PF, Edwards SJ, Parkinson IJ, Leat PT (2000) Geochemistry and tectonic significance of peridotites from the South Sandwich arc-basin system, South Atlantic. Contrib Mineral Petrol 139:36–53. https://doi.org/10.1007/s004100050572

Pearce JA, Kempton PD, Nowell GM, Noble SR (1999) Hf–Nd element and isotope perspective on the nature and provenance of mantle and subduction components in western Pacific arc–basin systems. J Petrol 40:1579–1611. https://doi.org/10.1093/petroj/40.11.1579

Pearson DG, Canil D, Shirey SB (2003) Mantle samples included in volcanic rocks: xenoliths and diamonds. In: Holland HD, Turekin KK (eds) The mantle and core. Treatise of geochemistry 2. Elsevier, Oxford, pp 171–275

Pedersen RB, Malpas J, Falloon T (1996) Petrology and geochemistry of gabbroic and related rocks from Site 894, Hess Deep. In: Mével C, Gillis KM, Allan JF, Meyer PS (eds) Proc ODP, Sci Results 147. College Station, TX, pp 3–19

Plank T, Langmuir CH (1998) The chemical composition of subducting sediment and its consequences for the crust and mantle. Chem Geol 145:325–394. https://doi.org/10.1016/S0009-2541(97)00150-2

Regelous M, Weinzierl CG, Haase KM (2016) Controls on melting at spreading ridges from correlated abyssal peridotite—mid-ocean ridge basalt compositions. Earth Planet Sci Lett 449:1–11. https://doi.org/10.1016/j.epsl.2016.05.017

Robinson JAC, Wood BJ, Blundy JD (1998) The beginning of melting of fertile and depleted peridotite at 1.5 GPa. Earth Planet Sci Lett 155:97–111. https://doi.org/10.1016/S0012-821X(97)00162-3

Sato H, Machida S, Kanayama S, Taniguchi H, Ishii T (2002) Geochemical and isotopic characteristics of the Kinan Seamount Chain in the Shikoku Basin. Geochem J 36:519–526. https://doi.org/10.2343/geochemj.36.519

Sanfilippo A, Dick HJB, Ohara Y, Tiepolo M (2016) New insights on the origin of troctolites from the breakaway area of the Godzilla Megamullion (Parece Vela back-arc basin): The role of melt mantle interaction on the composition of the lower crust. Isl Arc 25:220–234. https://doi.org/10.1111/iar.12137

Sanfilippo A, Dick HJB, Ohara Y (2013) Melt-rock reaction in the mantle: mantle troctolites from the Parece Vela ancient back-arc spreading center. J Petrol 54:861–885. https://doi.org/10.1093/petrology/egs089

Sen A, Snow JE, Ohara Y, Hirauchi K-I, Koketsu Y, Sanfilippo A, Basch V, Harigane Y, Fujii M, Okino K, Akizawa N (under review) Melting and evolution of amphibole-rich back-arc abyssal peridotites at the Mado Megamullion, Shikoku Basin

Snow JE, Dick HJB (1995) Pervasive magnesium loss by marine weathering of peridotite. Geochim Cosmochim Acta 59:4219–4235. https://doi.org/10.1016/0016-7037(95)00239-V

Stolper E, Newman S (1994) The role of water in the petrogenesis of Mariana trough magmas. Earth Planet Sci Lett 121:293–325. https://doi.org/10.1016/0012-821X(94)90074-4

Stracke A, Hofmann AW, Hart S (2005) FOZO, HIMU, and the rest of the mantle zoo. Geochem Geophys Geosyst 6:Q05007. https://doi.org/10.1029/2004GC000824

Sun SS, McDonough WF (1989) Chemical and isotopic systematics of oceanic basalts: implications for mantle composition and processes. In: Saunders AD, Norry MJ (eds) Magmatism in the ocean basins. Special Publications 42. Geological Society, London, pp 313–345

Tagawa M, Nakakuki T, Tajima F (2007) Dynamical modeling of trench retreat driven by the slab interaction with the mantle transition zone. Earth Planet Space 59:65–74. https://doi.org/10.1186/BF03352678

Tatsumi Y, Suzuki-Kamata K (2014) Cause and risk of catastrophic eruptions in the Japanese Archipelago. Proc Jpn Acad Ser B 90:347–352. https://doi.org/10.2183/pjab.90.347

Taylor B, Martinez F (2003) Back-arc basin basalt systematics. Earth Planet Sci Lett 210:481–497. https://doi.org/10.1016/S0012-821X(03)00167-5

Toplis MJ, Carroll MR (1996) Differentiation of ferro-basaltic magmas under conditions open and closed to oxygen: implications for the Skaergaard Intrusion and other natural systems. J Petrol 37:837–858. https://doi.org/10.1093/petrology/37.4.837

Tucholke BE, Behn MD, Buck WR, Lin J (2008) Role of melt supply in oceanic detachment faulting and formation of megamullions. Geology 36:455–458. https://doi.org/10.1130/G24639A.1

Tunheng A, Hirata T (2004) Development of signal smoothing device for precise elemental analysis using laser ablation-ICP-mass spectrometry. J Anal at Spectrom 19:932–934. https://doi.org/10.1039/B402493A

Van der Hilst R, Seno T (1993) Effects of relative plate motion on the deep structure and penetration depth of slabs below the Izu-Bonin and Mariana island arcs. Earth Plane Sci Lett 120:395–407. https://doi.org/10.1016/0012-821X(93)90253-6

Warren JW (2016) Global variation in abyssal peridotite compositions. Lithos 248–251:193–219. https://doi.org/10.1016/j.lithos.2015.12.023

Woodhead JD, Hergt JM (2001) Strontium, neodymium and lead isotope analyses of NIST glass certified reference materials: SRM 610, 612,

614. Geostand Newsl 25:261–266. https://doi.org/10.1111/j.1751-908X.2001.tb00601.x

Workman RK, Hart SR (2005) Major and trace element composition of the depleted MORB mantle (DMM). Earth Planet Sci Lett 231:53–72. https://doi.org/10.1016/j.epsl.2004.12.005

Yokoyama TD, Suzuki T, Kon Y, Hirata T (2011) Determination of rare earth element abundance and U-Pb age of zircons using multisport laser ablation-inductively coupled plasma mass spectrometry. Anal Chem 83:8892–8899. https://doi.org/10.1021/ac2012448

Yoshikawa M, Nakamura E (2000) Geochemical evolution of the Horoman peridotite complex: implications for melt extraction, metasomatism, and compositional layering in the mantle. J Geophys Res 105:2879–2901. https://doi.org/10.1029/1999JB900344

Zellmer GF, Sakamoto N, Matsuda N, Iizuka Y, Moebis A, Yurimoto H (2016) On progress and rate of the peritectic reaction Fo $+$ SiO$_2$ $\rightarrow$ En in natural andesitic arc magmas. Geochim Cosmochim Acta 185:383–393. https://doi.org/10.1016/j.gca.2016.01.005

Publisher's Note